

**Cover sheet for 'Response of atmospheric convection to surface drying:
new insights from isentropic analysis'**

Author 1: Laurel Régibeau-Rockett (Stanford University and National Research Council,
laurelregibeau@gmail.com)

Author 2: Morgan O'Neill (University of Toronto, morgan.oneill@utoronto.ca)

*This Work has been submitted to Journal of the Atmospheric Sciences. Copyright in this
Work may be transferred without further notice.*

1 **Response of atmospheric convection to surface drying: new insights from**
2 **isentropic analysis**

3 Laurel Régibeau-Rockett^{a,b} and Morgan E O'Neill^c

4 ^a *Department of Earth System Science, Stanford University, Stanford, California, USA*

5 ^b *National Research Council, Monterey, California, USA*

6 ^c *Department of Physics, University of Toronto, Toronto, Canada*

7 *Corresponding author: Laurel Régibeau-Rockett, laurelregibeau@gmail.com*

8 ABSTRACT: There is strong evidence that the atmospheric moisture content of several solar
9 system planets, including Earth, has varied over their lifetimes. A growing body of work also
10 documents a range of atmospheric water vapor content on exoplanets. An improved understanding
11 of the coupling between atmospheric moisture availability and convection could yield greater
12 intuition about the past and current states of planetary atmospheres, including Earth's atmosphere.
13 In this work, we investigate the changing heat engine behavior of localized radiative-convective
14 equilibrium convection in a suite of moist-to-nearly-dry numerical simulations. Each simulation
15 has a constant surface relative humidity, with values ranging from saturated to nearly dry surface
16 conditions. We observe a deepening of the planetary boundary layer and a corresponding lifting
17 of the cloud base as the surface dries, in agreement with previous numerical and observational
18 studies. The primary factor contributing to this is the reduction in the temperature of the lifting
19 condensation level implied by the Clausius-Clapeyron relationship. Additionally, the mass transport
20 by atmospheric convection increases in drier conditions, consistent with prior work. Finally,
21 inspection of the atmospheric circulation in the typical temperature-entropy space used for heat
22 engine analysis implies that the temperature of convective tops is invariant under surface drying
23 in our main suite of simulations, although this result is sensitive to the planetary boundary layer
24 parameterization.

25 **1. Introduction**

26 It has long been accepted that moisture is an essential aspect of atmospheric convection on Earth.
27 Compared to a dry atmosphere, for example, a moist atmosphere contains more intense updrafts
28 due to latent heat release, and has narrower convective updrafts compared to the downwelling area.
29 More recent work has demonstrated the far-reaching extent of atmospheric moisture's impacts on
30 convection: Pauluis and Held (2002a) and Pauluis (2011) argued the atmosphere acts both as a
31 heat engine that converts the atmosphere's differential heating into convective motions and as a
32 dehumidifier. These two aspects of atmospheric convection are in competition with each other,
33 with the atmosphere's action as a dehumidifier dominating over its behavior as a heat engine in
34 an idealized moist atmosphere comparable to our own (Pauluis and Held 2002a). This contradicts
35 the assumed dominance of the atmosphere's heat engine behavior in previous theories of moist
36 convection (Rennó and Ingersoll 1996; Emanuel and Bister 1996).

37 The amount of moisture in our atmosphere has likely varied significantly over Earth's lifetime.
38 For example, the Snowball Earth hypothesis posits that during the coldest portions of Earth's life-
39 time—particularly during subsets of the Neoproterozoic Era (1000–538.8 million years ago)—the
40 Earth's surface was covered by an extensive layer of ice (e.g. Kirschvink 1992; Hoffman et al.
41 1998; Evans et al. 1997). Such an ice-covered surface combined with the cold atmosphere would
42 imply a low atmospheric moisture content. Beyond Earth, mounting evidence suggests that moist
43 convection may be important to the past and current evolution of solar system atmospheres, such
44 as Venus (Kasting 1988), Mars (e.g. Wordsworth et al. 2013; Urata and Toon 2013), and Saturn (Li
45 and Ingersoll 2015). Recent observations of exoplanets have also found significant levels of atmo-
46 spheric water vapor (e.g. Tsiaras et al. 2019; Benneke et al. 2019; Roy et al. 2023; Mikal-Evans et al.
47 2023; Piaulet-Ghorayeb et al. 2024; Benneke et al. 2024). For example, many recent studies have
48 focused on the atmospheric composition of the exoplanet K2-18b, with most studies in agreement
49 that water vapor represents on the order of 0.01%-10% of its atmosphere by volume (e.g. Tsiaras
50 et al. 2019; Benneke et al. 2019; Madhusudhan et al. 2020; Changeat et al. 2019). The number
51 of observed exoplanets with expected water-containing atmospheres is likely to grow significantly,
52 with several exoplanets considered as candidates for harboring significant water (e.g. Southworth
53 et al. 2017; Cadieux et al. 2022; Piaulet et al. 2023; Cadieux et al. 2024). It seems likely that a large
54 range of water-containing atmospheres exist in our universe, with varying amounts of atmospheric

55 moisture. Understanding the impact of atmospheric moisture content on the characteristics of
56 atmospheric convection could help us better understand the past evolution and present state of an
57 array of different planetary atmospheres in the solar system and beyond—and most importantly,
58 our Earth’s atmosphere.

59 Previous work has demonstrated that more broadly, the atmospheric abundance of a condensable
60 component is important to atmospheric convective characteristics (e.g. Mitchell et al. 2006; Hueso
61 and Sánchez-Lavega 2006; Barth and Rafkin 2007; Pierrehumbert and Ding 2016; Mitchell and
62 Lora 2016; Ding and Pierrehumbert 2016). While this condensable substance is water on Earth,
63 this may not be the case on other planets. For example, Mitchell (2008) demonstrated, using
64 axisymmetric simulations of Titan’s atmosphere, that the atmosphere’s characteristics are strongly
65 sensitive to the initial supply of methane, which is the condensable component on Titan. The
66 author found that below a threshold amount of initial methane, Titan’s atmosphere abruptly shifted
67 into a warmer state with much less precipitation and a shallower, more asymmetric Hadley cell.
68 An investigation of the effect of atmospheric moisture on convective characteristics may have
69 implications for convection in planetary atmospheres containing a condensable component that is
70 not water.

71 A common idealized framework used to study the behavior of localized atmospheric convection
72 is that of radiative-convective equilibrium (RCE). In the idealized modelling context, the term
73 RCE refers to the statistically steady state of an idealized simulated atmosphere that experiences
74 both net radiative cooling and surface heating. To date, a few studies have examined the changes
75 in atmospheric behavior between moist and dry RCE. Pauluis and Held (2002a,b) compared the
76 characteristics of convection between moist and dry RCE in a cloud permitting model (CPM)
77 using an entropy budget. In addition, both Mrowiec et al. (2011) and Wang and Lin (2020, 2021)
78 studied differences in the properties of tropical cyclones between moist and dry RCE frameworks.
79 A comparison of the characteristics of moist and dry RCE convection was also performed by Singh
80 and O’Neill (2022).

81 The moist-to-dry transition itself has been extensively studied over both an ocean lower boundary
82 (e.g. Mitchell et al. 2006, 2009; Zsom et al. 2012; Fan et al. 2021; McKinney et al. 2022; McKinney
83 and Mitchell 2024) and land surfaces (Rochetin et al. 2014; McColl and Tang 2024; van der Drift
84 and O’Gorman 2025). For example, Pauluis (2000) performed an entropy budget of moist-to-

85 dry oceanic RCE convection in a CPM. The author found that from an energetic perspective,
86 atmospheric convection retains moist behavior for the majority of the moist-to-dry transition, until
87 the atmospheric moisture content has decreased by roughly 90%. This moist regime is characterized
88 by the dominance of the energetic consumption of moist processes over the kinetic energy of
89 convective motions and a greater portion of the total mechanical work dissipation occurring in
90 shear zones surrounding falling hydrometeors rather than via the turbulent cascade. Later, Alland
91 et al. (2017) investigated the impact of midlevel dry-air entrainment on oceanic tropical cyclones by
92 applying Pauluis and Mrowiec (2013)'s technique of isentropic analysis to a suite of CPM ensembles
93 initialized with different levels of atmospheric moisture. The ensembles initially had the same sea
94 surface temperature and an identical subcloud vapor mixing ratio, but had different values of
95 the initial moist entropy deficit above this point. The authors found no significant differences in
96 the impacts of mid-level entrainment on the entropy of the eyewall updraft under atmospheric
97 drying. However, the convective mass transport of the overturning circulation decreased under
98 atmospheric drying, implying that dry mid-level air may impact the tropical cyclone circulation
99 via entrainment into the inflow layer. Another study by Spaulding-Astudillo and Mitchell (2023)
100 varied the atmospheric saturation vapor pressure by a constant scaling factor in a suite of 1-D RCE
101 simulations over an oceanic lower boundary. A decreased saturation vapor pressure resulted in
102 lower, warmer high cloud tops and a deeper planetary boundary layer. Finally, Cronin and Chavas
103 (2019) investigated the moist-to-dry transition of atmospheric convection for the specific case of
104 tropical cyclones over the ocean. The authors found that their simulated tropical cyclones exhibited
105 a more gradual transition from moist to dry characteristics compared to the findings of Pauluis
106 (2000), although it should be noted that no tropical cyclones formed for their simulations with
107 mid-to-low values of atmospheric moisture.

108 Some key differences exist between these moist-to-dry studies of Pauluis (2000) and Cronin
109 and Chavas (2019), which could explain the contrast in the sharpness of the transition from moist
110 to dry atmospheric behavior found in these works. First, whereas Pauluis (2000) investigated
111 the moist-to-dry behavior of disorganized atmospheric convection, Cronin and Chavas (2019)
112 studied tropical cyclones, which are highly organized systems. Organized convective systems
113 may experience the moist-to-dry transition quite differently from localized convection. Second,
114 Pauluis (2000) examined the moist-to-dry transition from the perspective of the atmosphere's

115 behavior as a heat engine, with a focus on its changing energetics, whereas Cronin and Chavas
116 (2019) examined changes in more “classical” tropical cyclone characteristics including the tropical
117 cyclone intensity and radius of maximum winds. Viewing atmospheric systems in terms of their
118 thermodynamic behavior as heat engines, rather than in terms of these classical characteristics,
119 could yield a different view on the changes in behavior of such systems over the transition. Finally,
120 the construction of the moist-to-dry transition was different in these two studies. Whereas Cronin
121 and Chavas (2019) varied the surface saturation specific humidity in their simulations, Pauluis
122 (2000) varied the saturation specific humidity of the whole atmosphere. Such differences in the
123 construction of the transition may have large impacts on the changing behavior of convection.
124 For example, as noted by Pauluis (2000), his construction of the moist-to-dry transition results in
125 hydrometeor fall velocities remaining at the same order of magnitude regardless of the reduction
126 in hydrometeor water mass. This may have a strong impact on the variability of atmospheric cloud
127 content as the atmosphere dries, resulting in an artificially steep decrease in cloud amounts. This
128 could significantly affect the variability of atmospheric convection over the transition.

129 Pauluis and Mrowiec (2013) developed the procedure of “isentropic analysis”. Isentropic anal-
130 ysis supports the computation of an alternative streamfunction of the atmospheric circulation cast
131 into height and equivalent potential temperature space. This space has greater relevance to the
132 thermodynamic behavior of the atmospheric heat engine compared to the classical Eulerian space
133 in which convective streamfunctions are typically constructed. As such, this method can provide a
134 new perspective on the response of atmospheric convection to changes in environmental thermo-
135 dynamics, including temperature and moisture changes. Several previous works have employed
136 isentropic analysis to study the behavior of atmospheric convection and convective systems in
137 different contexts (e.g. Singh and O’Gorman 2015; Pauluis 2016; Mrowiec et al. 2016; Muller and
138 Romps 2018; O’Neill and Chavas 2020; Li et al. 2023; Régibeau-Rockett et al. 2024). For exam-
139 ple, some studies have employed a version of isentropic averaging developed for tropical cyclones
140 (Mrowiec et al. 2016) to study the impacts of drying above the lifting condensation level on the
141 secondary circulation of tropical cyclones (Alland et al. 2017), the evolution of tropical cyclones
142 from an energetic perspective (Fang et al. 2019; Li et al. 2023), and tropical cyclone energetics
143 in the mature state (Pauluis and Zhang 2017). Isentropic averaging has also been applied to both
144 localized atmospheric convection (e.g. Pauluis and Mrowiec 2013; Pauluis 2016) and to organized

145 convective systems (e.g. Mrowiec et al. 2015; Dauhut et al. 2017) to yield new understanding on the
146 behavior of these systems. For example, Pauluis (2016) found that a doubling of the atmospheric
147 carbon dioxide concentration results in a larger convective entropy transport. This results in an
148 increase in the total energy production by the convective heat engine, although the partitioning
149 of this energy between moist processes and the kinetic energy of convective motions does not
150 significantly change.

151 In this study, we apply isentropic analysis to a suite of RCE CPM simulations with varying levels
152 of surface moisture, where the moisture transition is constructed by varying the surface saturation
153 mixing ratio as in Cronin and Chavas (2019). The goal of this analysis is to investigate how the
154 thermodynamic behavior of localized convection varies as the available surface moisture decreases
155 from fully moist conditions, without rotation. The paper is structured as follows: in section 2
156 we describe our suite of simulations and the analysis methodology, including a summary of the
157 isentropic analysis method. In section 3, we present the results of our analyses. Finally, we provide
158 a discussion of our results in section 4 and present some conclusions in section 5.

159 **2. Methods**

160 *a. Model description*

161 In this work, we analyze changes in atmospheric behavior in a suite of moist-to-near-dry simula-
162 tions conducted using the Cloud Model 1 (CM1, Bryan and Fritsch 2002), version 21.1. In general,
163 the design of our simulations emulates Singh and O’Gorman (2016), who performed an entropy
164 budget on a suite of simulations over different sea surface temperatures in CM1 version 16 with
165 added alterations. Their modifications to CM1 and the design of their suite of simulations had the
166 goal of conserving energy and mass well enough that their entropy budget could be closed within
167 an acceptable margin of error. Although we do not perform an entropy budget in our work, we
168 adopt a similar simulation design with the goal of improving the model’s conservation of energy
169 and mass.

170 All simulations are in a non-rotating $84 \text{ km} \times 84 \text{ km}$ doubly-periodic domain. This domain
171 size is smaller than the 200-300 km domain size required to support self-aggregation (Muller and
172 Held 2012; Jeevanjee and Romps 2013). The domain has a 1-km horizontal grid spacing and a
173 vertically stretched grid spacing (Wilhelmson and Chen 1982) ranging from 50 m at a height of

174 0 km to 500 m from 5.5 km up to the model top at 27 km. A Rayleigh damping layer is imposed
 175 in the top 3 km. The simulations are run with CM1’s mesoscale modelling setup and the Yonsei
 176 University (YSU) planetary boundary layer parameterization (Hong et al. 2006). Microphysics
 177 is parameterized using the Morrison six-species double-moment scheme (Morrison et al. 2005,
 178 2009) with hail as the large ice category. The radiation scheme is the RRTMG interactive scheme.
 179 Following Bretherton et al. (2005), we remove the diurnal and seasonal cycles from the radiative
 180 scheme via fixing the solar constant at 650.83 W m^{-2} and the solar zenith angle at 50.5° . We
 181 employ a Smagorinsky parameterization scheme for horizontal turbulence (Bryan and Rotunno
 182 2009), a sixth-order hyper-diffusion scheme, and a sixth-order nondiffusive advection scheme. As
 183 in Singh and O’Gorman (2016), the sea surface temperature is set to 301.5 K. The simulations
 184 include dissipative heating and employ a set of equations for the moist microphysics that improves
 185 the conservation of energy and mass by accounting for the heat capacity of hydrometeors (Bryan
 186 and Fritsch 2002) and including the vertical transport of energy associated with hydrometeor
 187 sedimentation.

188 The surface layer in our simulations is parameterized following the Weather Research and
 189 Forecasting model (WRF, Skamarock et al. 2008) MM5 scheme (Grell et al. 1994), as modified by
 190 Jiménez et al. (2012). We varied the surface dryness in our simulations by adding a scaling factor
 191 β to the surface saturation mixing ratio in the latent heat flux formula of the surface layer model
 192 following previous studies of the moist-to-dry transition (Mitchell et al. 2006, 2009; Cronin and
 193 Chavas 2019; Fan et al. 2021; McKinney et al. 2022):

$$LHF = \rho_1 L_{v,s} C_q U (\beta r_s^* - r_{v,1}). \quad (1)$$

194 Here, ρ_1 (kg m^{-3}) and $r_{v,1}$ (kg kg^{-1}) are the dry-air density and water vapor mixing ratio,
 195 respectively, in the surface layer (Jiménez et al. 2012). In CM1, this corresponds to the lowest
 196 model level of 25 m. U is the horizontal wind speed (m s^{-1}) at 10 m enhanced by a convective
 197 velocity as in Beljaars (1995) and a subgrid velocity following Mahrt and Sun (1995), r_s^* (kg kg^{-1})
 198 is the saturation water vapor mixing ratio at the surface, and C_q is the dimensionless bulk transfer

199 coefficient. The term $L_{v,s}$ (J kg^{-1}) is the latent heat of vaporization at the surface, defined as:

$$L_{v,s} = L_{v,0} + (c_{p,v} - c_{p,l})(T_s - T_{ref}),$$

200 where T_s (K) is the surface temperature, $L_{v,0}$ (J kg^{-1}) is the latent heat of vaporization at
201 a reference temperature T_{ref} of 273.15 K, and $c_{p,v}$ and $c_{p,l}$ are, respectively, the specific heat
202 capacities ($\text{J kg}^{-1} \text{K}^{-1}$) of water vapor and liquid water.

203 The term β in Eq. (1) is a dimensionless constant and controls the amount of available moisture
204 that can exit the surface. This quantity can be thought of as the surface relative humidity and is
205 related to the surface evaporative resistance, $\mathcal{R} = 100 \times (1 - \beta)$ (McKinney et al. 2022). A value
206 of 1 corresponds to a typical surface moisture supply given the sea surface temperature of 301.5 K
207 (i.e., a saturated or “fully moist” surface), whereas a low value is equivalent to a surface with a high
208 evaporative resistance. Surface conditions resulting in a high evaporative resistance could include
209 a high salinity and limited water (Fan et al. 2021). We vary the value of the β parameter from 1 to
210 0.1 over the suite of simulations, which allows us to investigate the impacts of surface drying on
211 localized RCE convection. We choose to examine a range of β values from 1 to no lower than 0.1
212 because simulations with lower values of β did not achieve an RCE state within an 100-day time
213 frame.

214 The simulations are initialized with small-amplitude thermal noise perturbations and vertical
215 profiles of potential temperature and moisture computed from a period of 10 statistically steady
216 days from the end of RCE simulations with an identical design and matching β values, but that
217 are initialized with the Dunion (2011) moist tropical sounding. A similar initialization method
218 was used in the moist-to-dry simulations of Cronin and Chavas (2019) and allows the system to
219 adjust to the imposed surface conditions. The initialization simulations have a model top of 28
220 km, 1 km higher than the domain height of the main suite of simulations. This is due to CM1’s
221 requirement that input soundings must extend higher than the chosen model top. The upper-level
222 Rayleigh damping layer thickness in these simulations matches that of the main set of simulations,
223 and so the damping layer begins 1 km higher in the initialization simulations.

224 A total of five simulations are conducted, with β set to 1, 0.75, 0.5, 0.25, and 0.1. Following
225 initialization simulations lasting between 32 and 83 days, with the time to RCE increasing as

226 β decreased, the simulations reached a statistical equilibrium after approximately 50 days (Fig.
 227 1). This RCE state was identified following the procedure described in Text S1 of the online
 228 supplemental materials. The presence of a statistically steady state after the point where RCE is
 229 first identified is confirmed by visual inspection of Hovmöller diagrams, constructed with daily
 230 data, of the vertical profile of equivalent potential temperature (θ_e) in each simulation (Fig. 1). In
 231 this work, θ_e is defined as in Bryan (2008) and following its formulation in CM1:

$$\theta_e = T \left(\frac{p_{ref}}{p_d} \right)^{\frac{R_d}{c_{p,d}}} \mathcal{H}^{-\frac{r_v R_v}{c_{p,d}}} \exp \left[\frac{r_v L_{v,0}}{c_{p,d} T} \right],$$

232 where T is the temperature (K), $p_{ref} = 1000$ hPa is the reference pressure, p_d is the partial
 233 pressure of dry air (hPa), R_d is the gas constant for dry air, $c_{p,d}$ ($\text{J kg}^{-1} \text{K}^{-1}$) is the specific heat
 234 capacity of dry air, r_v is the water vapor mixing ratio (kg kg^{-1}), and \mathcal{H} is the relative humidity
 235 with respect to liquid water:

$$\mathcal{H} = \frac{e_p}{e_s},$$

236 where e_p is the water vapor pressure (Pa) and e_s (Pa) is the saturation vapor pressure of Bolton
 237 (1980).

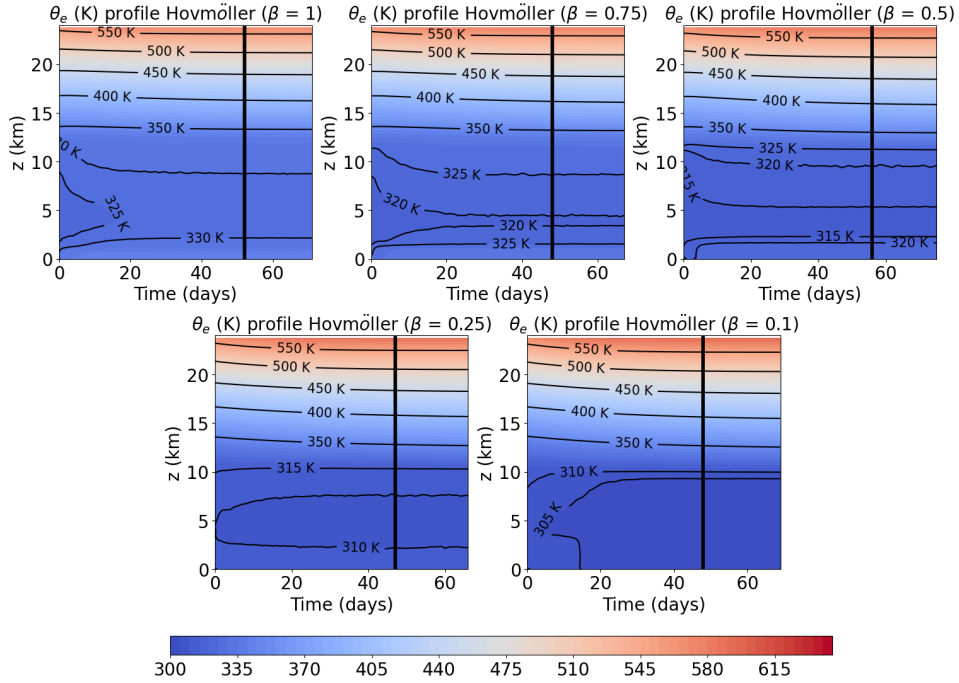
238 Once statistical equilibrium was achieved, we ran the simulations for a further 20 days with
 239 output data every 4 hours. The beginning of each of these 20-day periods is denoted by the vertical
 240 black lines in Fig. 1. In what follows, we apply isentropic analysis to these 20-day periods, as will
 241 be described in section 2b.

245 *b. A Summary of Isentropic Analysis*

246 In this work, we apply the isentropic analysis procedure to 20-day steady-state periods from each
 247 of the simulations described above. In our work, isentropic analysis is broken into the following
 248 steps (Pauluis 2016):

- 249 1. Compute the isentropic-average¹ vertical mass flux $\langle \rho w \rangle(z, \theta_e)$ ($\text{kg m}^{-2} \text{s}^{-1} \text{K}^{-1}$) following
 250 Eq. (1) of Pauluis and Mrowiec (2013). $\langle \rho w \rangle$ is the time- and horizontal-average of the

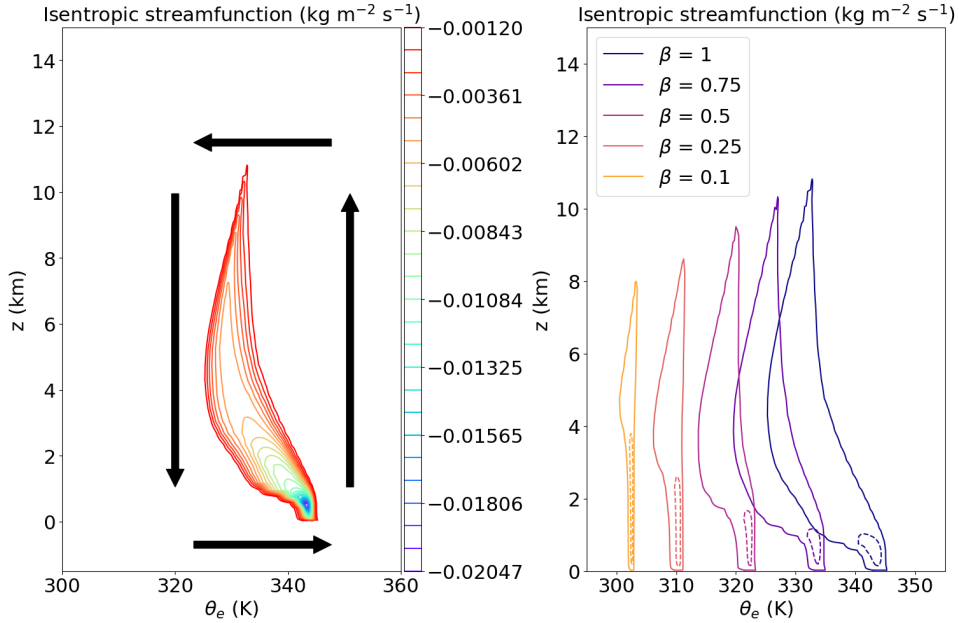
¹Although the standard nomenclature for this and other procedures involved in isentropic analysis uses the term “isentropic”, these computations do not involve constant-entropy conditions.



242 FIG. 1. Hovmöller plots of the time- and horizontal-mean vertical profiles of equivalent potential temperature
 243 (colors) in each constant- β simulation. Values from within the model sponge layer are not shown. The black
 244 vertical line denotes the start of the 20-day steady-state period that we analyze for each simulation.

251 vertical mass flux at a given height z that was binned by the corresponding equivalent potential
 252 temperature value θ_e .

- 253 2. Use $\langle \rho w \rangle$ to compute the isentropic streamfunction $\psi(z, \theta_e)$ (Fig. 2) following Eq. (3)
 254 of Pauluis and Mrowiec (2013). For given values of z and θ_e , $\psi(z, \theta_e)$ is the cumulative
 255 isentropic-average upward mass flux for equivalent potential temperature values less than or
 256 equal to θ_e .
- 257 3. Use the isentropic streamfunction to construct a set of representative thermodynamic trajec-
 258 tories. When plotted as a contour plot with N levels, $\psi(z, \theta_e)$ is represented as a set of closed
 259 loops in $z - \theta_e$ space (Fig. 2). The isentropic analysis method implicitly assumes that these
 260 closed loops represent the mean trajectories of real air parcels in the atmospheric system.
 261 This assumption was shown to hold reasonably well in the context of axisymmetric tropical
 262 cyclones in Régibeau-Rockett et al. (2024).



270 FIG. 2. Left: Isentropic streamfunction, $\psi(z, \theta_e)$, obtained from the 20-day steady state period of the $\beta =$
 271 1 simulation. Black arrows show the direction of the thermally direct overturning circulation in $z - \theta_e$ space.
 272 Right: Comparison of the deepest trajectories (solid lines) derived from ψ during the 20-day steady-state period
 273 of each simulation. Also shown are the median trajectories (dashed lines).

- 263 4. Compute the mass-weighted isentropic-average values of thermodynamic quantities f , such
 264 as the absolute temperature and moist entropy: $\tilde{f} = \langle \rho f \rangle / \langle \rho \rangle$.
- 265 5. Interpolate these mass-weighted isentropic-average thermodynamic quantities \tilde{f} onto the
 266 constructed trajectories. The result is a projection of the isentropic streamfunction into
 267 different thermodynamic spaces, such as temperature-entropy space. Projecting the isentropic
 268 streamfunction into different spaces in this way can provide a new perspective on the influence
 269 of environmental changes on the atmospheric convection.

274 3. Results

275 In this section, we present the results of applying the isentropic analysis to 20-day steady-
 276 state periods from each of the constant- β simulations. We begin by presenting the transition
 277 of the atmospheric circulation in response to surface drying viewed in terms of the isentropic

278 streamfunction. This streamfunction is then projected into different thermodynamic spaces, which
279 yields additional insight on the changing behavior of the atmospheric circulation over the transition.

280 Because our work investigates the impact of the atmospheric moisture content on convective
281 dynamics, our results may be sensitive to our choice of microphysical scheme. We checked the
282 sensitivity of our results to the microphysics parameterization by running two suites of simulations
283 identical to those discussed in section 2, but that had different representations of microphysics:
284 the first suite employed the Thompson microphysics scheme (Thompson et al. 2008; Thompson
285 and Eidhammer 2014), whereas the second used the double-moment graupel-and-hail NSSL mi-
286 crophysics parameterization (Ziegler 1985; Mansell et al. 2010; Mansell and Ziegler 2010). We
287 also examined the sensitivity of our results to the planetary boundary layer (PBL) parameterization
288 in two suites of sensitivity simulations. The first suite used the Mellor-Yamada-Nakanishi-Niino
289 (MYNN) level 2.5 PBL scheme (Nakanishi and Niino 2006, 2009; Olson et al. 2019), while the
290 second used the NCEP Global Forecast System scheme (GFS-EDMF, Hong and Pan 1996). More
291 information on these sensitivity tests, together with the results of analyzing these four simulation
292 suites, can be found in Texts S2 and S3 and in Table 1. In general, we find that the results presented
293 in this section are not sensitive to the microphysical or PBL schemes. Henceforth, we will note
294 instances where our results are qualitatively sensitive to these parameterizations.

312 *a. Effects of Moisture on the Isentropic Streamfunction*

313 Figure 2 presents changes in selected trajectories from the isentropic streamfunction over the suite
314 of simulations. We show here changes in both the deepest trajectory and a median trajectory, defined
315 as the twelfth of 25 levels used to plot ψ in step 3 of the isentropic averaging process described in
316 section 2b. The changes in the isentropic streamfunction reveal changes in the characteristics of the
317 atmospheric circulation: first, as the surface dries, the depth of the circulation decreases (Table 1).
318 In addition, the range of equivalent potential temperatures sampled by the circulation decreases,
319 with more similar values of θ_e for updrafts and downwelling air (Table 1). This is unsurprising,
320 since a smaller difference in θ_e between rising and sinking air is characteristic of dry convection.
321 As β decreases, we also observe an increase in the depth of the PBL, or equivalently an increase in
322 the lifting condensation level (LCL) (Table 1). In Fig. 2, the LCL is the level at which the θ_e range
323 of the isentropic circulation noticeably increases, with the PBL below represented by the region in

295 TABLE 1. Changes in different metrics from the $\beta = 1$ simulation to the $\beta = 0.1$ simulation. The metrics
296 are: diagnosed cloudtop height (z_{top}) and temperature (T_{top}); mean difference in θ_e and vapor mixing ratio
297 between updrafts and downdrafts for the deep trajectory ($\theta_{e,u-d}$ and $r_{v,u-d}$); percentage difference between
298 vertical profiles of the relative humidity derived from the updraft and the downdraft of the deep trajectory below
299 the diagnosed lifting condensation level (LCL) ($\mathcal{H}_{GG,u-d,PBL}$), where the percentage difference is computed
300 with respect to the downdraft profile and the relative humidity is with respect to both liquid water and ice as in
301 Goff and Gratch (1946); height and temperature of the diagnosed LCL (z_{LCL} and T_{LCL}); height and temperature
302 of the tropopause (z_{trop} and T_{trop}); near-surface Gibbs free energy of water vapor ($g_{v,surf}$); change in moist
303 entropy and total mixing ratio from the diagnosed LCL to the diagnosed cloudtop for the deep trajectory (δs_{up}
304 and $\delta r_{T,up}$); change in Gibbs free energy of water vapor from the surface to the diagnosed LCL during the updraft
305 leg of the deep trajectory ($\delta g_{v,LCL-surf}$); isentropic mass circulation ($\Delta\psi$), mean anomalous upward vertical
306 mass flux within and above the PBL ($\Delta\rho w'_{PBL}$ and $\Delta\rho w'_{non-PBL}$); net radiative cooling (Q_{rad}); surface sensible
307 and latent heat fluxes (SHF and LHF); and mean precipitation rate. Except $\mathcal{H}_{GG,u-d,PBL}$, all percentages are
308 computed with respect to the value of each metric in the $\beta = 1$ simulation. Some results that depend on θ_e are
309 recomputed using Marquet (2011)'s entropy potential temperature. Because not all results will be impacted by
310 this change, only those that could be affected are shown. Due to the shape of the trajectories yielded by this
311 method (Fig. S33), δs_{up} may not accurately capture changes in the entropy for deep convective updrafts.

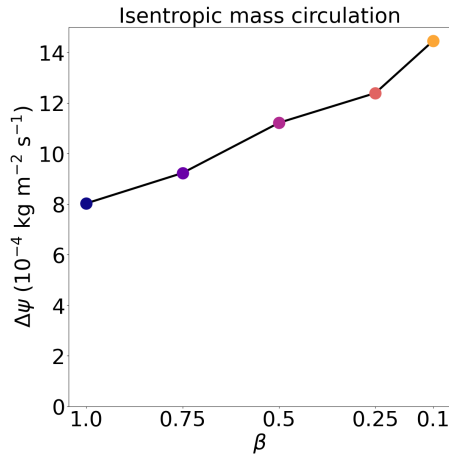
Metric	Main	Thompson	NSSL	MYNN	GFS	Marquet
Δz_{top} (km)	-2.8	-2.5	-3.1	-3.5	-3.5	-
$\Delta\theta_{e,u-d}$ (%)	-81	-78	-80	-83	-86	-74
Δz_{LCL} (km)	3.0	3.0	3.1	3.1	3.2	3.4
$\Delta(\Delta\psi)$ (%)	80	83	121	151	240	133
ΔQ_{rad} (%)	-54	-56	-49	-57	-55	-
$\Delta Q_{rad} $ (W m^{-2})	-49	-47	-42	-54	-51	-
Δ SHF (W m^{-2})	28	27	31	27	29	-
Δ LHF (W m^{-2})	-78	-74	-74	-75	-79	-
$\Delta\rho w'_{PBL}$ (%)	2000	1900	3800	2400	3100	-
$\Delta\rho w'_{non-PBL}$ (%)	-36	-10	-24	-62	-8.0	-
ΔT_{LCL} (K)	-31	-33	-34	-33	-33	-
$\Delta\delta s_{up}$ (%)	-95	-91	-91	-96	-97	62
$\Delta r_{v,u-d}$ (%)	-79	-78	-79	-81	-84	-
$\Delta\delta r_{T,up}$ (%)	-86	-84	-85	-87	-86	-
Δ precipitation rate (%)	-95	-99	-98	-95	-96	-
$\Delta\mathcal{H}_{GG,u-d,PBL}$ (%)	10	9.3	9.8	9.7	5.6	-
$\Delta\delta g_{v,LCL-surf}$ (%)	600	600	620	610	540	-
$\Delta g_{v,surf}$ (%)	530	500	500	540	480	-
ΔT_{top} (K)	1.5	-2.3	2.1	7.3	7.6	-
ΔT_{trop} (K)	-1.6	0.69	0.37	-0.36	0.058	-
Δz_{trop} (km)	-2.5	-3.0	-3.0	-2.5	-2.5	-

324 which rising air has a similar equivalent potential temperature value as sinking air. This is because
325 the LCL is the level at which latent heat begins to be released by rising air parcels. Here, the
326 LCL's height is diagnosed based on the characteristics of the isentropic streamfunction and is not
327 necessarily equivalent to the thermodynamic LCL.

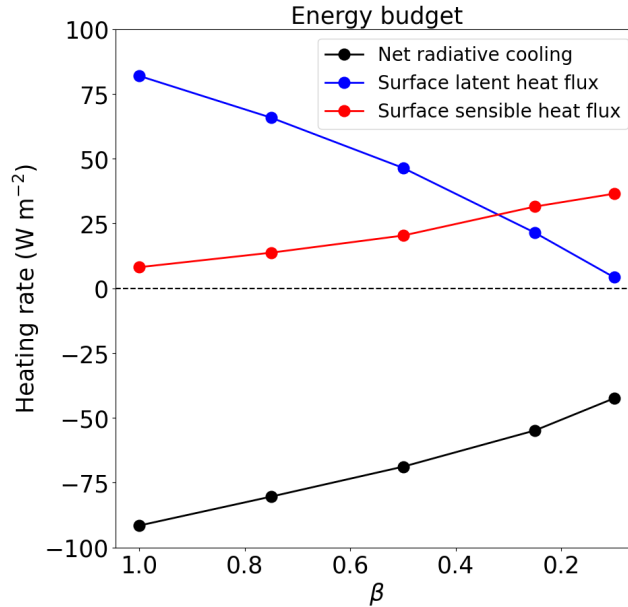
328 We next study the variability of the isentropic mass transport, $\Delta\psi$ ($\text{kg m}^{-2} \text{s}^{-1}$). The quantity
329 $\Delta\psi$ is the mass transport in each of the N levels of the isentropic streamfunction, defined following
330 Pauluis (2016) as $\Delta\psi = -N^{-1}\psi_{min}$, where ψ_{min} is the minimum value of ψ . By construction, this
331 is the same for each level of the isentropic streamfunction. As can be seen in Fig. 3, $\Delta\psi$ increases
332 by 80% between the fully moist and driest simulations (Table 1). Note that the percentage change
333 in mass circulation is computed with respect to its value in the fully moist simulation. Because
334 $\Delta\psi$ represents the mass transport of each level of the isentropic streamfunction, with high- θ_e air
335 rising and low- θ_e air sinking, the increase in $\Delta\psi$ should indicate an increase in the convective heat
336 transport. However, in our simulations, the radiative cooling rate and total surface heat flux in the
337 domain, computed as described in the appendix, decrease strongly as the surface dries (Fig. 4,
338 Table 1). In RCE, these quantities are balanced by the convective heat transport, implying that the
339 heat transport also decreases as the atmosphere dries. This is not incompatible with the increase in
340 the convective mass transport because the heat transport is also dependent on the difference in θ_e
341 between the updraft and downwelling air. This difference decreases significantly with decreasing
342 β (Fig. 2, Table 1), and so acts to decrease the convective heat transport. Overall, the decrease in
343 the updraft/downwelling θ_e difference outweighs the increased convective mass transport in terms
344 of its impact on the convective heat transport, resulting in the lower convective heat transport
345 that we observe under surface drying. It is interesting to note, however, that the decline in the
346 external heating and cooling of the atmosphere under drying is sufficiently slow compared to the
347 narrowing of the updraft-downdraft difference in θ_e that the circulation must intensify to maintain
348 a sufficiently large convective heat transport.

354 Although the convective mass transport increases overall, shallow and deep convection may
355 respond quite differently to imposed surface drying. We next examine changes in the mean upward
356 anomalous mass flux², $\rho w'^+$, for the PBL and for the region above the PBL separately (Fig. 5,
357 Table 1). The former is a proxy for changes in shallow convection, while the latter represents
358 changes in the deep convective mass flux. Here, the PBL height is not diagnosed based on the

²Here, the anomalous mass flux is computed with respect to the horizontal-mean vertical mass flux.

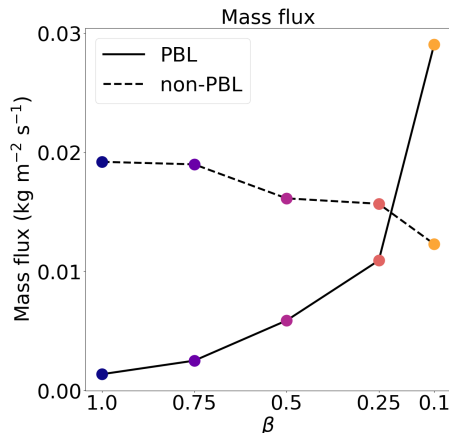


349 FIG. 3. Isentropic mass circulation $\Delta\psi$, computed during the 20-day steady-state periods from each simulation,
 350 versus β .



351 FIG. 4. Time-mean, domain-integrated radiative heating rate divided by the area of the surface (black line),
 352 and time- and horizontal-mean surface latent (blue line) and sensible (red line) heat fluxes, computed during the
 353 20-day steady-state periods from each simulation, versus β .

359 characteristics of the isentropic streamfunction as in the rest of the text. Instead, we use the PBL
 360 height that is output from CM1. The mass transport by shallow convection strongly increases under
 361 surface drying, while the mass transport by deep convection decreases. Hence, the increase in the
 362 isentropic mass circulation is the result of a strong increase in shallow convective mass transport.



363 FIG. 5. Mean upward anomalous vertical mass flux within the PBL (solid line) and excluding the PBL (dashed
 364 line), computed during the 20-day steady-state periods from each simulation, versus β .

365 As discussed in Marquet (2017), the isentropic streamfunction may have different characteristics
 366 depending on the definition of the equivalent potential temperature, which could impact the robust-
 367 ness of our results that depend on the isentropic streamfunction. Given this, we examined changes
 368 with surface drying in the deepest and median trajectories from the isentropic streamfunction, with
 369 this streamfunction computed using Marquet (2011)’s entropy potential temperature θ_s (Text S4,
 370 Table 1). With one exception, noted in the text, the trends discussed in this text under surface
 371 drying are not qualitatively sensitive to the definition of the equivalent potential temperature. An
 372 additional minor difference between our main results and those obtained with θ_s is that it is not
 373 clear that the difference in the entropy potential temperature between the updraft and the downdraft
 374 decreases under surface drying, with the exception of the driest experiment (Fig. S33).

375 *b. Surface Drying Transition in Other Thermodynamic Spaces*

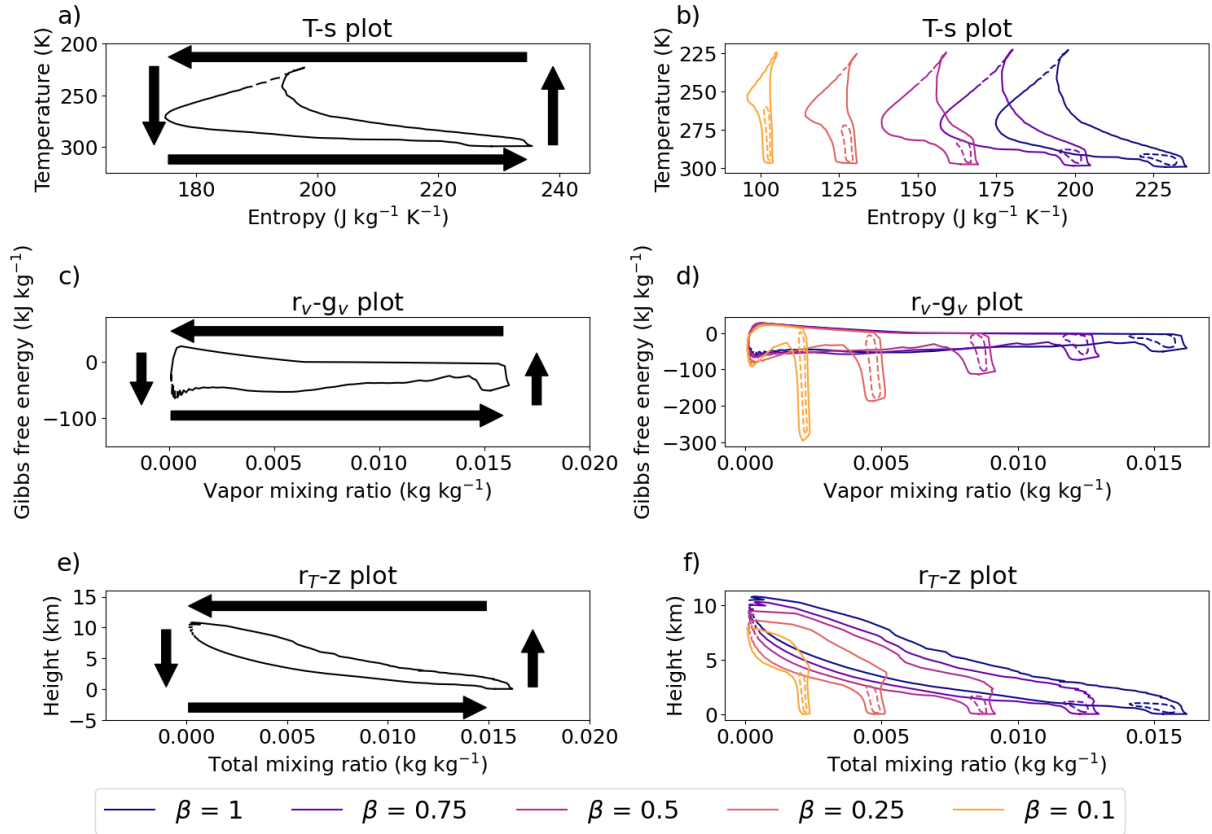
376 Figure 6 presents the response to surface drying of the isentropic streamfunction projected into
 377 three thermodynamically-relevant spaces: temperature-entropy (Fig. 6a, b), vapor mixing ratio-
 378 vapor Gibbs free energy (Fig. 6c, d), and height-total mixing ratio space (Fig. 6e, f). All quantities
 379 are defined as in Régibeau-Rockett et al. (2024). Here, the increase in the total mixing ratio
 380 during subsidence (Fig. 6e) is due to mixing of the subsiding air with cloudy air due to convective
 381 detrainment, as well as re-evaporation of precipitation in the free troposphere (Pauluis 2016). Note
 382 also that the Gibbs free energy of water vapor g_v can be approximated as $g_v \approx R_v T \log \mathcal{H}$ (Pauluis

383 2011). The term g_v is primarily dependent on changes in \mathcal{H} (Pauluis 2016), and is close to zero at
 384 saturation and negative/positive for unsaturated/supersaturated air. For example, in the simulation
 385 with $\beta=1$ (Fig. 6c), the unsaturated near-surface air is represented by the portion of the deep
 386 trajectory with $g_v \approx -50 \text{ kJ kg}^{-1}$ and the vapor mixing ratio r_v increasing from roughly 0.015 to
 387 0.016 kg kg^{-1} . The LCL is the point at which air rising upwards from the surface at relatively
 388 constant r_v reaches the point past which g_v is close to zero, representing the saturated updraft.
 389 Atmospheric convection involves the removal of water at a higher (near-zero) Gibbs free energy
 390 than the value of g_v at which water is added via surface evaporation (Pauluis 2011, 2016). This
 391 separation results in irreversible entropy production that reduces the mechanical work output from
 392 the atmospheric heat engine (Pauluis 2011, 2016).

393 The projection of ψ into height-total mixing ratio ($z - r_T$) space (Fig. 6e,f) demonstrates in
 394 greater detail the increase in height of the diagnosed LCL—represented by the height at which
 395 the range of the total vapor mixing ratio r_T (kg kg^{-1}) increases markedly between the updraft and
 396 the downdraft—over the transition. As can be seen in the temperature-entropy plot (Fig. 6b), the
 397 temperature at which the entropy range of the circulation experiences a large growth decreases with
 398 increased surface drying. This implies that the temperature of the LCL diminishes with decreasing
 399 β (Table 1). This is in line with Bolton (1980)’s formula for the temperature of the LCL implied
 400 by the temperature dependence of the saturation vapor pressure. The decrease in the temperature
 401 and increase in height of the LCL in response to surface drying is confirmed by inspection of the
 402 horizontal- and time-mean vertical profiles of temperature in the simulations (Fig. 7). Here, the
 403 diagnosed LCL is the point above which the lapse rate becomes less negative with height due to
 404 the latent heat released in convective updrafts.

412 The sharp decrease in the updraft entropy of the deep trajectory above the LCL in temperature-
 413 entropy space (Fig. 6a) is likely representative of the exchange of water mass between the updraft
 414 and its environment due to convective entrainment and detrainment (Pauluis 2016). In tropical
 415 cyclones, the eyewall updraft air experiences a very small decrease in its entropy due to little dry-air
 416 entrainment occurring during ascent (Pauluis and Zhang 2017). For our simulations, the decrease
 417 in updraft entropy, δs_{up} , is much weaker for lower values of β ³ (Fig. 6b, Table 1), which could
 418 represent a decrease in convective entrainment and detrainment. Another possible explanation

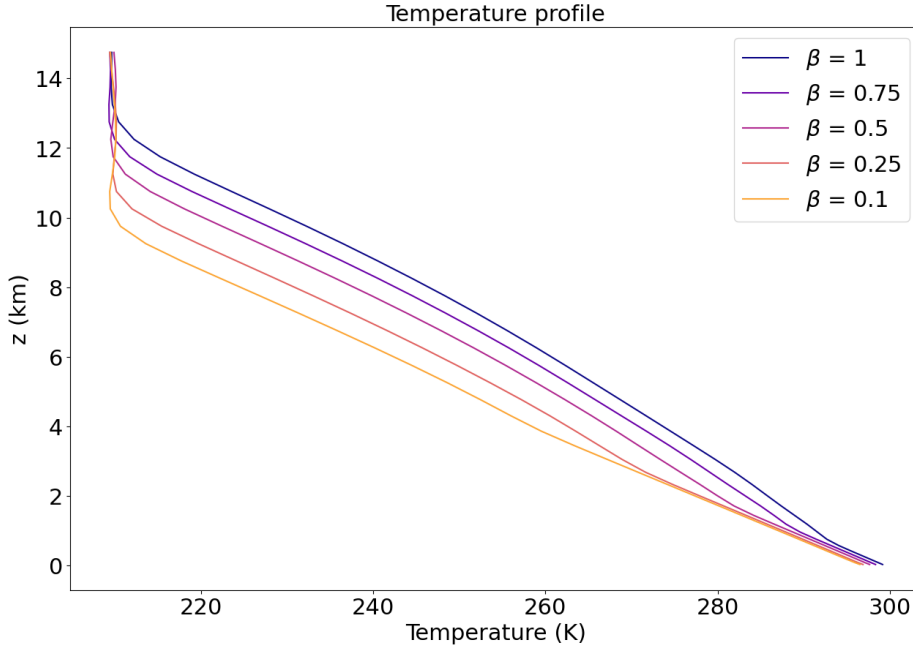
³This metric instead increases under drying for the moist entropy of Marquet (2011) (Table 1). However, because of the shape of the Marquet (2011) temperature-entropy trajectories this metric may not be appropriate for measuring the total change in entropy during the updraft (Fig. S33).



405 FIG. 6. Left: Isentropic streamfunction, $\psi(z, \theta_e)$, from the $\beta = 1$ simulation projected into a) temperature-
 406 entropy space, c) vapor mixing ratio-vapor Gibbs free energy space, and e) height-total water mixing ratio space.
 407 Black arrows show the direction of the thermally direct overturning circulation. Right: Comparison of the deepest
 408 (solid lines) and median (dashed lines) trajectories derived from ψ for each simulation in b) temperature-entropy
 409 space, d) vapor mixing ratio-vapor Gibbs free energy space, and f) height-total water mixing ratio space.

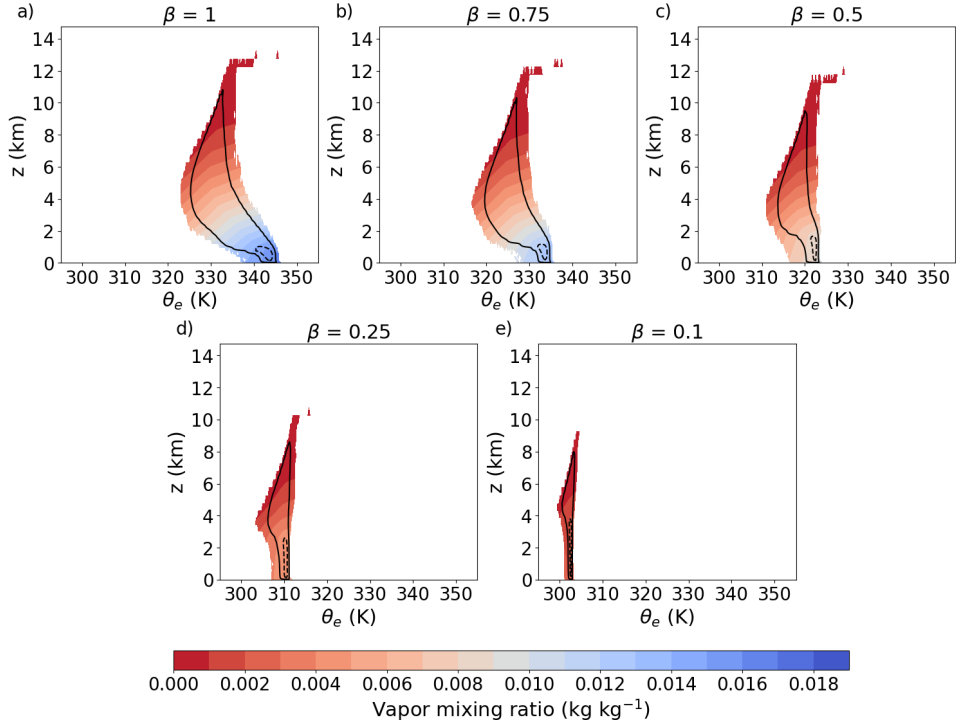
419 is that these processes occur, but do not substantially change the entropy of the updraft air as a
 420 consequence of a more uniform atmospheric humidity distribution. Fig. 8 shows the changes in
 421 the isentropic-average vapor mixing ratio as the surface dries, together with the deep and median
 422 trajectories from the isentropic streamfunction. The humidity gradient between the rising and
 423 descending branches of the circulation strongly decreases as β is lowered (Table 1). Because our
 424 analysis cannot quantify changes in convective entrainment, it is possible that the entrainment rate
 425 also varies under surface drying.

429 The smaller decrease of r_T during the upward branch of the deep trajectory in $z - r_T$ space implies
 430 a lower precipitation rate in the drier simulations (Fig. 6f, Table 1). This is confirmed by inspection

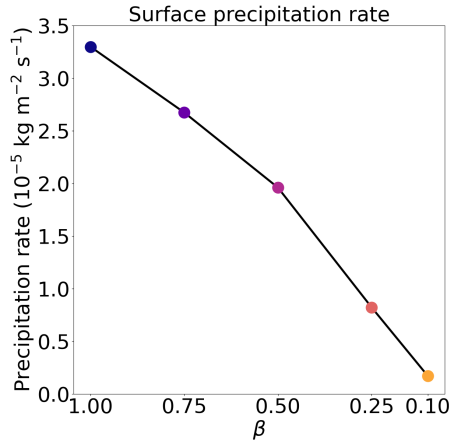


410 FIG. 7. Time- and horizontal-mean vertical profiles of absolute temperature (K) from the 20-day steady-state
 411 periods in each constant- β simulation.

431 of the time- and horizontal-average surface precipitation rate in the constant- β simulations (Fig.
 432 9, Table 1), which decreases by 95% from the fully moist simulation to the simulation in which β
 433 = 0.1. However, because the surface drying also results in a deeper and drier PBL, this does not
 434 necessarily imply a reduction in precipitation re-evaporation in the PBL. We examined changes
 435 in the mean percentage difference in the relative humidity (\mathcal{H}_{GG})—defined with respect to both
 436 ice and liquid water as in Goff and Gratch (1946) and Régibeau-Rockett et al. (2024)—between
 437 the PBL portions of the updraft and downdraft branches of the deepest isentropic streamfunction
 438 trajectory (Table 1). Here, the percent difference is computed with respect to the relative humidity
 439 of the downdraft profile. The updraft profile is assumed to represent the PBL below convective
 440 clouds while the downdraft profile represents the state of the PBL far from convective updrafts. A
 441 larger difference between the updraft and downdraft profiles should then correspond to more re-
 442 evaporation of precipitation in the regions near convective clouds. The relative humidity difference
 443 increases by 10% from the fully moist simulation to the driest simulation. This implies that surface
 444 drying results in more PBL re-evaporation of precipitation.



426 FIG. 8. Comparison of the mass-weighted isentropic-average vapor mixing ratio (colors), and the deepest and
 427 median trajectories from ψ for the simulations with $\beta =$ a) 1, b) 0.75, c) 0.5, d) 0.25, and e) 0.1. All quantities
 428 are computed during the 20-day steady-state periods from each simulation.



445 FIG. 9. Time- and horizontal-mean precipitation rate, computed during the 20-day steady-state periods from
 446 each simulation, versus β .

447 Over the transition from moist to nearly dry, the change in g_v between the surface and the
 448 updraft strongly increases (Fig. 6d, Table 1). As the relative humidity of the surface—the source

449 of moisture to the atmosphere—decreases, the irreversibility associated with surface evaporation
450 grows significantly, represented by the increasingly negative value of g_v near the surface (Table
451 1). Both the near-surface g_v and the irreversible entropy production from surface evaporation (e.g.
452 Singh and O’Gorman 2016) depend on $\log \mathcal{H}_s$, where \mathcal{H}_s is the relative humidity with respect to
453 liquid water at the surface. A small decrease in \mathcal{H}_s results in a large increase in the irreversible
454 entropy production from surface evaporation and a strongly negative near-surface g_v .

455 Finally, comparison of the deep trajectories in Fig. 6b reveals that although under surface
456 drying the atmospheric circulation becomes shallower in terms of its maximum height, the range
457 of temperatures experienced by the circulation remains very steady as β lowers (Table 1). This
458 is consistent with a decrease in the tropopause height in the simulations with drier atmospheres,
459 which is confirmed to occur by inspection of the mean vertical profiles of temperature in the
460 simulations (Fig. 7, Table 1). Note that the range of temperatures sampled by the deep trajectories
461 is not constant under drying in our two PBL scheme sensitivity tests (Text S3), as will be elaborated
462 in the next section.

463 4. Discussion

464 *a. Convective mass transport and energetics*

465 The growth in the overall convective mass transport that we observe as the surface dries is in
466 line with the findings of previous CPM studies of disorganized oceanic RCE convection (Pauluis
467 2000; Pauluis and Held 2002a; Singh and O’Neill 2022). Pauluis and Held (2002a) and Singh and
468 O’Neill (2022) compare moist and dry RCE simulations, finding that at a height of 4 km, convective
469 updrafts are more ubiquitous in their model domains in dry RCE compared to moist RCE. The drier
470 simulations of Pauluis (2000) also show widespread and stronger updrafts compared to moister
471 simulations. This could correspond to a larger overall convective mass transport. Pauluis and Held
472 (2002a) additionally find that the turbulent dissipation of kinetic energy—which in a steady state is
473 equal to the rate of kinetic energy work associated with convective motions—is much larger in dry
474 RCE than in moist RCE, in line with the strong increase in the mean dissipation rate under drying
475 in our simulations (not shown). This metric is strongly related to the mass transport by convection,
476 and so this finding is in agreement with the larger convective mass transport that we find in our
477 drier simulations.

478 However, our results are qualitatively different from those of previous studies investigating the
479 impacts of atmospheric drying on tropical cyclones. Alland et al. (2017) find that the convective
480 mass transport by the tropical cyclone eyewall updraft decreases as the initial amount of moisture
481 above the LCL decreases over their suite of simulation ensembles. Meanwhile, Mrowiec et al.
482 (2011) and Cronin and Chavas (2019) both observe decreases in the eyewall updraft velocity in
483 dry tropical cyclones compared to moist simulations of these storms. The contrast between the
484 response of tropical cyclone updrafts and localized convective updrafts to atmospheric drying may
485 represent a difference in the response of tropical cyclones, which are highly organized convective
486 systems, to changes in atmospheric moisture compared to the response of disorganized convection.
487 It is possible that the behavior of other organized convective systems, such as mesoscale convective
488 systems or extratropical cyclones, may follow more closely the response of tropical cyclones to
489 surface drying than the changing behavior of disorganized convection that we observe. A study
490 comparing the impacts of surface drying on organized convective systems to the response of
491 disorganized convection to the same change has not been attempted to date.

492 A larger convective mass transport under surface drying also contrasts with the results of van der
493 Drift and O’Gorman (2025)’s terrestrial simulations. The authors investigate changes in terrestrial
494 disorganized convection under an increased vegetative evaporative resistance. A higher surface
495 temperature is imposed for drier conditions in order to hold the free-tropospheric temperature
496 constant. The authors find that the upward convective mass flux is smaller for their drier simula-
497 tions. The imposed increase in the surface temperature accompanying drying complicates a direct
498 comparison between this study and ours. However, this contrast implies that the convective mass
499 flux may respond differently to atmospheric drying over land compared to over the ocean.

500 We next compare our results to those of large-scale moist-to-dry studies. Mitchell et al. (2009)
501 investigate the response of the Hadley Cell to a combination of surface drying and a reduction in
502 the relative humidity threshold for convection. They find that the Hadley Cell is more intense in
503 drier conditions, which may imply an increased mass transport, in line with our results. However,
504 McKinney et al. (2022) observe that the Hadley Cell’s intensity does not significantly change
505 in response to surface drying. The authors also investigate the effect of a reduced atmospheric
506 saturation vapor pressure on the Hadley Cell, finding in this case that its intensity is weaker under

507 drier conditions. The discrepancy between these results could imply a dependence of the change
508 in the mass transport on the form of applied atmospheric drying, as will be discussed in section 5.

509 In this work, the increase in the convective mass transport occurs despite a reduction in the total
510 convective heat transport implied by the decreases we observe in the total surface heat flux and net
511 radiative cooling at lower β values. A decrease in the total surface heat flux is observed in dry RCE
512 compared to moist RCE by both Pauluis and Held (2002a) and Singh and O’Neill (2022). McColl
513 and Tang (2024)’s terrestrial RCE study also demonstrates that column radiative cooling is lower
514 under surface drying. Additionally, Wang and Lin (2021) find that dry tropical cyclones experience
515 less radiative cooling than moist tropical cyclones. Pauluis (2000) investigates these changes in
516 greater detail and observes a gradual decrease in the net radiative heat loss of the atmosphere over
517 a suite of moist-to-dry RCE simulations, although it should be noted that the author employs a
518 simpler Newtonian cooling scheme for radiation compared to our fully interactive radiative scheme.

519 *b. Vertical structure of the circulation*

520 In our experiments, surface drying results in a deepening of the PBL. This increase in the
521 boundary layer depth is in line with results of previous observational studies, which generally find
522 that the daily-maximum height of the PBL is largest over drier regions, such as Australia, the Sahara,
523 and the western United States (Seidel et al. 2012; von Engel n and Teixeira 2013; Zhang et al. 2020).
524 This result is additionally consistent with the study of Wang and Lin (2020), who find that dry
525 tropical cyclones have a deeper inflow layer compared to moist tropical cyclones. Because tropical
526 cyclone inflow occurs in the tropical cyclone boundary layer, this implies that this layer was deeper
527 in their dry experiment than under moist conditions. The deepening of the PBL is also supported
528 by several moist-to-dry studies over ocean (Zsom et al. 2012; Fan et al. 2021; Spaulding-Astudillo
529 and Mitchell 2023) and land lower boundaries (van der Drift and O’Gorman 2025). For example,
530 in the 1-D cloud model investigation of Zsom et al. (2012) the authors find, using an Earth-like
531 configuration of their model, that a lower atmospheric relative humidity causes liquid water clouds
532 to form at higher elevations, implying a deeper PBL. Spaulding-Astudillo and Mitchell (2023)
533 also observe a deepening of the PBL in response to atmospheric drying, accompanied by a higher
534 LCL. In our simulations, the PBL deepens under surface drying because the LCL is higher. The
535 temperature-dependent constraint on the mass fraction of atmospheric water vapor (Bolton 1980)

536 predicts that the LCL will be cooler and therefore higher in a drier atmosphere. This is in line with
537 the lower LCL temperature in our drier simulations. A similar explanation is briefly provided by
538 Seidel et al. (2012) to explain the deeper PBLs they identify in the drier U.S. compared to Europe.

539 We also find that the simulations with lower β values have lower tropopause heights (Fig. 7).
540 Cronin and Chavas (2019) find an increase of the pressure of the tropopause with surface drying in
541 their moist-to-dry simulations, although this does not necessarily imply a decrease in the tropopause
542 height. Similarly, Spaulding-Astudillo and Mitchell (2023) observe that the height above which the
543 magnitude of the atmospheric lapse rate significantly decreases is lower in their drier experiments,
544 implying a reduced tropopause height. A lower tropopause in dry compared to moist RCE is
545 observed by Singh and O’Neill (2022) in their simulations of localized convection. Specifically,
546 the authors find that the tropopause is roughly 5 km lower in their dry simulation compared to the
547 moist simulation. Assuming a linear scaling of the tropopause height with surface drying, this
548 would correspond to a decrease of 4.5 km from fully moist conditions to those corresponding to
549 our simulation with $\beta = 0.1$. In comparison, the height of the lapse-rate tropopause (WMO 1957)
550 in our simulations, computed as in Xian and Homeyer (2019), decreases by 2.5 km between the
551 fully moist and driest simulations (Table 1). This is substantially less than the estimated decrease
552 given the results of Singh and O’Neill (2022). This may indicate that the majority of the transition
553 towards a fully dry temperature lapse rate—and an associated decrease in the tropopause—chiefly
554 occurs at low values of atmospheric moisture below the range studied here. It is also possible that
555 this results from the differences in the construction of Singh and O’Neill (2022)’s moist and dry
556 simulations compared to our surface relative humidity scaling. Finally, we note that Pauluis (2000)
557 does not observe a consistently-signed change in the height of the tropopause with atmospheric
558 drying: for experiments in which the whole atmosphere’s specific humidity is reduced to 50% and
559 5% of its fully moist value, respectively, the tropopause height decreases as the atmosphere dries,
560 in line with our results. However, when the specific humidity is further reduced from 5% to 0.5%
561 of its fully moist value, the tropopause height increases as the atmosphere becomes drier. The
562 lowest value of β examined in our simulations is above the range at which Pauluis (2000) observes
563 a reversal in the tropopause height’s response to surface drying. It is possible that we would find
564 non-monotonicity in our simulations if we examined lower β values.

565 The deepening PBL combined with the lower tropopause result in much shallower atmospheric
566 convection in our drier experiments. This is consistent with the shallower convection found in dry
567 RCE compared to moist RCE by Pauluis and Held (2002a) and Singh and O’Neill (2022). Several
568 studies of the moist-to-dry transition also observe that atmospheric convection becomes shallower
569 in drier conditions (Mitchell et al. 2006; McKinney et al. 2022; Spaulding-Astudillo and Mitchell
570 2023). Additionally, Mrowiec et al. (2011) and Cronin and Chavas (2019) find that the overturning
571 circulation of their simulated tropical cyclones is shallower in dry or near-dry RCE than in moist
572 RCE.

573 Although the precipitation rate decreases under surface drying in our simulations, our results
574 imply that the re-evaporation of precipitation in the PBL increases under surface drying, in line with
575 the results of van der Drift and O’Gorman (2025)’s terrestrial study. As discussed by the authors,
576 the larger re-evaporation of precipitation likely occurs because it falls through a much deeper
577 and drier PBL in the simulations with lower β values. The authors additionally find substantial
578 decreases in the precipitation efficiency under drying as a result of the increased re-evaporation,
579 which likely also occurs in our simulations.

580 *c. Convective-top temperature*

581 A projection of the isentropic streamfunction into temperature-entropy space reveals that for the
582 deepest convective trajectories, the temperature difference between the surface and convective tops
583 is largely insensitive to changes in the surface moisture. The surface temperature was constant
584 across our simulations, so this invariance is equivalent to a lack of variation in the minimum tem-
585 perature achieved by the deepest convective trajectories with surface drying (Table 1). Because the
586 minimum temperature of convective clouds typically occurs at the cloud top, this implies that the
587 cloud top temperature is approximately constant with varying surface moisture in our simulations.
588 Hartmann and Larson (2002) introduced the Fixed Anvil Temperature (FAT) hypothesis, which
589 argues that the temperature of tropical cloud anvils remains fixed regardless of the surface temper-
590 ature. Although some studies have challenged the existence of FAT and proposed alternatives (e.g.
591 Zelinka and Hartmann 2010; Igel et al. 2014; Seeley et al. 2019), several numerical modeling and
592 observational studies have supported FAT (e.g. Xu et al. 2005; Kuang and Hartmann 2007; Eitzen
593 et al. 2009; Khairoutdinov and Emanuel 2013; Singh and O’Gorman 2015), and the hypothesis has

594 been extended from the context of the tropics to the global atmosphere (Thompson et al. 2017).
595 Although the FAT hypothesis was developed for the context of an atmosphere under an increasing
596 surface temperature, its arguments may be applicable to cloud anvil temperature variability under
597 varying surface moisture. This is because the main arguments of FAT are based on the following
598 (Hartmann and Larson 2002):

- 599 • The Clausius-Clapeyron relation places a temperature-dependent constraint on atmospheric
600 moisture content.
- 601 • Clear-sky radiative cooling in the troposphere is dominated by longwave emission from water
602 vapor.
- 603 • A maximum decrease of clear-sky radiative cooling with height (occurring at around the level
604 where the atmospheric water vapor content becomes negligible, assuming the first and second
605 listed points are valid) creates a maximum in clear-sky convergence, which must be balanced
606 by strong convective divergence.

607 The first and third statements above should hold true regardless of the total amount of moisture at
608 the surface and in the atmosphere itself. The second argument may not be valid in an atmosphere
609 with sufficiently low water vapor, or in one in which constituents other than water vapor make
610 major contributions to radiative cooling. However, for an atmosphere without such alternative
611 emitters the invariance of the lowest temperature experienced by convection across our simulations
612 suggests that the FAT hypothesis might be applicable to the atmosphere over different levels of
613 surface moisture. This is somewhat consistent with the results of Thuburn and Craig (2002), who
614 find in a simple radiative-convective model without explicit convection that the temperature of the
615 convective top is approximately constant with decreasing atmospheric relative humidity down to
616 a relative humidity of 40%, beyond which the convective top temperature grows with decreasing
617 relative humidity.

618 Although our results imply that the temperature of convective tops is constant as the surface dries
619 in the main suite of simulations, this result is not robust to the choice of PBL scheme (Text S3).
620 Indeed, in both sets of PBL sensitivity simulations, the lowest temperature sampled by the deep
621 trajectories increases by roughly 7-8 K from the fully moist to the driest simulations (Table 1). This
622 is qualitatively in line with the increase in the temperature of convective tops found by Thuburn

623 and Craig (2002) over the atmospheric moist to dry transition, although our sensitivity experiments
624 do not support their finding that the convective-top temperature is invariant for higher values of
625 atmospheric moisture content ($\beta \geq 0.5$) (Text S3). Spaulding-Astudillo and Mitchell (2023) also
626 observe that the temperature at the peak high cloud fraction increases under atmospheric drying.
627 Prior studies employing both the YSU and MYNN PBL parameterizations have largely found
628 support for FAT under varying surface temperatures (Satoh et al. 2012; Tsushima et al. 2014;
629 Cesana et al. 2017; Ohno and Satoh 2018; Núñez Ocasio and Dougherty 2024), implying that
630 validation of this hypothesis is not dependent on the choice of PBL scheme. An extension of FAT
631 to the context of varying surface moisture has not previously been investigated in detail, and taken
632 together our results are inconclusive regarding whether such an extension is valid. Future studies
633 should use methods other than isentropic analysis to investigate whether the FAT hypothesis might
634 be extended to situations besides varying surface temperature, such as varying surface moisture.

635 5. Conclusions

636 In this work, we investigated the changing characteristics of moist convection subjected to
637 surface drying from the thermodynamic perspective of the convective isentropic streamfunction.
638 Our findings are as follows: as the surface dries, the separation in the entropy of convective updraft
639 air and downwelling air decreases (Fig. 2, Table 1). This is accompanied by an increase in the
640 convective mass transport and a deepening of the PBL (Figs. 2, 3 and 6f, Table 1). Meanwhile,
641 the total heating and cooling of the atmosphere, represented by the surface total heat fluxes and
642 domain-integrated net radiative cooling, decrease as the parameter β decreases (Fig. 4, Table 1),
643 implying a reduction in the heat transport by convection. The convective heat transport is dependent
644 on both the mass transport by convection and the difference in equivalent potential temperature
645 between the updraft and downdraft. Although the convective mass transport increases in drier
646 conditions, this does not contradict the inferred decrease in the convective heat transport because
647 there is a strong reduction in the updraft/downdraft equivalent potential temperature difference
648 under surface drying.

649 Further insight into the response of convection to surface drying is gained by projecting the isen-
650 tropic streamfunction into various thermodynamic spaces (Fig. 6, Table 1), such as temperature-
651 entropy space (Fig. 6a,b). The weakening gradient of entropy along the updraft of the deepest

652 trajectories of the isentropic streamfunction in the drier simulations is indicative of lessening
653 exchange of water mass with the environment due to entrainment and detrainment. This par-
654 tially results from a decreasing gradient of water vapor between the updraft and its surroundings.
655 However, our analysis cannot determine whether entrainment and detrainment rates change under
656 surface drying. We additionally find that for the deepest convective trajectories, the temperature
657 at the top of the circulation is insensitive to surface drying, although this result is not robust to the
658 choice of PBL parameterization. Combined with the lowering height of the tropopause, this results
659 in the atmosphere containing shallower convection in our drier simulations. Other findings of this
660 work include that surface drying results in a reduced precipitation rate, increased re-evaporation of
661 precipitation in the PBL, greater irreversibility associated with surface evaporation, and a reduction
662 in the temperature of the LCL.

663 This work includes several idealizations that may limit the applicability of our findings to real
664 atmospheric convection. First, our simulations are conducted over an oceanic lower boundary.
665 The agreement of our results with most of the findings of terrestrial RCE studies (McColl and
666 Tang 2024; van der Drift and O’Gorman 2025) implies that our work may capture some of
667 the convective changes resulting from atmospheric drying over land. However, there are many
668 important differences between land and ocean lower boundary conditions, even in highly idealized
669 models. Future work should verify whether the convective changes in response to atmospheric
670 drying that we see here are generalizable to atmospheres over land. Second, the behavior of
671 convection in response to atmospheric drying discussed here may depend on the surface layer
672 parameterization employed in our study. Future work should verify whether our results are robust
673 under alternative surface schemes. Additionally, the simulations analyzed here are designed based
674 on the characteristics of Earth’s current atmosphere. Although it is possible that our results could
675 be generalized to the atmospheres of other planets with significant amounts of atmospheric water
676 vapor or another condensable component, ensuing studies should verify whether our findings hold
677 true when the similarity of the simulated atmosphere to Earth’s is relaxed.

678 Our simulations were conducted in a small domain to prevent convective self-aggregation from
679 occurring. We chose to exclude self-aggregated convection from our analysis because organized
680 convective systems such as self-aggregated convection may respond quite differently to surface
681 drying than disorganized convection. Compared to disorganized convection, convective updrafts

682 in aggregated systems are more shielded, on average, from mixing with the drier non-convecting
683 environment because the near-plume environment is moister (e.g. Grabowski and Moncrieff 2004;
684 Tompkins and Semie 2017; Becker et al. 2018). As such, the effects of atmospheric drying may have
685 less of an impact on organized convection compared to the disorganized convection studied here.
686 Aggregated convection also contains fewer high clouds and more low clouds than disorganized
687 convection (e.g. Tobin et al. 2012; Wing and Cronin 2016; Bony et al. 2016). Hence, the response
688 of aggregated convective systems to imposed drying may be more weighted towards changes in
689 low clouds than deep convective clouds. Finally, the degree of convective self-aggregation may
690 vary under surface drying. All of these factors could complicate the interpretation of our results.
691 This small-domain study allowed us to examine the fundamental convective response to surface
692 drying. However, our results may not apply to organized convective systems or large-domain RCE,
693 which supports convective self-aggregation. Indeed, some of our results differ from the findings
694 of moist-to-dry studies of tropical cyclones—highly organized systems—although the majority are
695 consistent with them. Future work should examine the response of organized convection, such as
696 self-aggregated convection, to changes in atmospheric moisture content.

697 We investigated the effects of atmospheric drying on convection through drying the surface
698 and allowing our simulations to come to a new, statistically steady RCE state. However, other
699 methodologies of atmospheric drying have been employed in the literature, such as reducing the
700 atmospheric saturation vapor pressure by a constant everywhere (Pauluis 2000; McKinney et al.
701 2022; Spaulding-Astudillo and Mitchell 2023; McKinney and Mitchell 2024). It is possible that
702 our results are sensitive to the form of the applied atmospheric drying. As discussed herein,
703 many of our results are supported by the findings of moist-to-dry studies that employed different
704 drying methodologies (Pauluis 2000; Zsom et al. 2012; Spaulding-Astudillo and Mitchell 2023).
705 For example, the results of both Spaulding-Astudillo and Mitchell (2023) and Pauluis (2000) are
706 broadly in agreement with ours, and are derived from suites of simulations in which the atmospheric
707 saturation vapor pressure was varied. As noted previously, two studies of the Hadley circulation
708 under drying disagree on how the Hadley cell’s intensity, which relates to the mass transport,
709 changes in drier conditions (Mitchell et al. 2009; McKinney et al. 2022). The sign and magnitude
710 of this change vary across the three different atmospheric drying methods employed in these studies.
711 This implies that the increase in convective mass transport that we observe may be sensitive to the

712 atmospheric drying approach. However, this does not seem likely as our result is in line with the
713 findings of Pauluis (2000), who uses a different drying method compared to our study. Instead,
714 the Hadley cell's response to drying may be more sensitive to the form of the applied atmospheric
715 drying compared to localized convection.

716 *Acknowledgments.* We are grateful to Olivier Pauluis, Noah Diffenbaugh, Leif Thomas, Aditi
717 Sheshadri, and Jonathan Mitchell for their helpful feedback on this manuscript. We are also
718 thankful to the Stanford Research Computing Center staff for their technical support during this
719 project, and for allowing us to carry out this study via the use of their high-performance computing
720 cluster. We are additionally grateful to George Bryan for creating and maintaining the CM1 model
721 code for the community. Some portions of this paper are published in thesis form in fulfillment of
722 the requirements for the Ph.D. (Régibeau-Rockett 2025).

723 *Data availability statement.* All simulations were run using the Cloud Model 1, version 21.1,
724 which is available at <https://www2.mmm.ucar.edu/people/bryan/cm1/>. Modified model
725 source code, as well as input and output files, is available at [https://doi.org/10.5281/](https://doi.org/10.5281/zenodo.17352676)
726 [zenodo.17352676](https://doi.org/10.5281/zenodo.17352676). Finally, our analysis code is located at [https://doi.org/10.5281/](https://doi.org/10.5281/zenodo.17352687)
727 [zenodo.17352687](https://doi.org/10.5281/zenodo.17352687).

728 APPENDIX

729 Computation of the energy budget

730 In a simulated RCE atmosphere, the total energy of the atmosphere is statistically steady and
731 conservation of energy requires that:

$$\overline{LHF} + \overline{SHF} + [Q_{rad}] = 0, \quad (\text{A1})$$

732 where \overline{X} denotes the time- and horizontal-mean value of X , and $[X]$ is equal to the time-average,
733 domain-integrated value of X divided by the area of the surface. The terms LHF and SHF (W
734 m^{-2}) are the bulk surface fluxes of latent and sensible heat, respectively, and Q_{rad} (W m^{-3}) is the
735 radiative heating rate per unit volume. The LHF is defined as in Eq. (1), and the SHF is computed
736 in the model as (Jiménez et al. 2012):

$$SHF = \rho_1 c_{p,d} C_h U (\theta_s - \theta_1).$$

737 Here, $c_{p,d}$ ($\text{J kg}^{-1} \text{K}^{-1}$) is the specific heat capacity of dry air at constant pressure, C_h is a
 738 dimensionless bulk transfer coefficient, and θ_s and θ_1 are, respectively, the potential temperature
 739 (K) at the surface and at the lowest model level.

740 The first law of thermodynamics under moist, constant-volume conditions states that:

$$dQ = \rho c_{v,m} dT, \quad (\text{A2})$$

741 where ρ (kg m^{-3}) is the dry-air density and $c_{v,m}$ ($\text{J kg}^{-1} \text{K}^{-1}$) is the heat capacity of humid air
 742 under constant-volume conditions, defined as in CM1:

$$c_{v,m} = c_{v,d} + c_{v,v}r_v + c_{p,l}r_l + c_{p,fr}r_{fr}.$$

743 Here, $c_{v,d}$ ($\text{J kg}^{-1} \text{K}^{-1}$) is the heat capacity of dry air under constant-volume conditions, $c_{v,v}$ (J
 744 $\text{kg}^{-1} \text{K}^{-1}$) is the heat capacity at constant volume of water vapor, and $c_{p,l}$ and $c_{p,fr}$ are the heat
 745 capacities of liquid and solid water under constant-pressure conditions ($\text{J kg}^{-1} \text{K}^{-1}$). The terms r_v ,
 746 r_l , and r_{fr} are the mixing ratios of water vapor, liquid water, and solid water (kg kg^{-1}).

747 In accordance with Eq. (A2), Q_{rad} is computed from the model-output time tendencies of
 748 temperature due to the longwave and shortwave forcings in the radiative scheme, $\dot{T}_{rad,SW}$ and
 749 $\dot{T}_{rad,LW}$, as:

$$Q_{rad} = \rho c_{v,m} (\dot{T}_{rad,SW} + \dot{T}_{rad,LW}). \quad (\text{A3})$$

750 References

- 751 Alland, J. J., B. H. Tang, and K. L. Corboseiro, 2017: Effects of Midlevel Dry Air on Development
 752 of the Axisymmetric Tropical Cyclone Secondary Circulation. *J. Atmos. Sci.*, **74**, 1455–1470,
 753 <https://doi.org/10.1175/JAS-D-16-0271.1>.
- 754 Barth, E. L., and S. C. R. Rafkin, 2007: TRAMS: A new dynamic cloud model for Titan's methane
 755 clouds. *Geophys. Res. Lett.*, **34**, L03 203, <https://doi.org/10.1029/2006GL028652>.
- 756 Becker, T., C. S. Bretherton, C. Hohenegger, and B. Stevens, 2018: Estimating bulk entrainment
 757 with unaggregated and aggregated convection. *Geophys. Res. Lett.*, **45**, 455–462, <https://doi.org/>

758 10.1002/2017GL076640.

759 Beljaars, A. C. M., 1995: The parametrization of surface fluxes in large-scale models under free
760 convection. *Quart. J. Roy. Meteor. Soc.*, **121**, 255–270, <https://doi.org/10.1002/qj.49712152203>.

761 Benneke, B., and Coauthors, 2019: Water Vapor and Clouds on the Habitable-zone Sub-
762 Neptune Exoplanet K2-18b. *The Astrophysical Journal Letters*, **887**, L14, [https://doi.org/](https://doi.org/10.3847/2041-8213/ab59dc)
763 [10.3847/2041-8213/ab59dc](https://doi.org/10.3847/2041-8213/ab59dc).

764 Benneke, B., and Coauthors, 2024: JWST Reveals CH₄, CO₂, and H₂O in a Metal-rich Miscible
765 Atmosphere on a Two-Earth-Radius Exoplanet. *arXiv astro-ph.EP 2403.03325 [Preprint]*, URL
766 <https://arxiv.org/abs/2403.03325>.

767 Bolton, D., 1980: The Computation of Equivalent Potential Temperature. *Mon. Wea. Rev.*, **108**,
768 1046–1053, [https://doi.org/10.1175/1520-0493\(1980\)108<1046:TCOEPT>2.0.CO;2](https://doi.org/10.1175/1520-0493(1980)108<1046:TCOEPT>2.0.CO;2).

769 Bony, S., B. Stevens, D. Coppin, T. Becker, K. Reed, A. Voigt, and B. Medeiros, 2016: Ther-
770 modynamic control of anvil cloud amount. *Proc. Natl. Acad. Sci. (USA)*, **113**, 8927–8932,
771 <https://doi.org/10.1073/pnas.1601472113>.

772 Bretherton, C. S., P. N. Blossey, and M. Khairoutdinov, 2005: An Energy-Balance Analysis of Deep
773 Convective Self-Aggregation above Uniform SST. *J. Atmos. Sci.*, **62**, 4273–4292, [https://doi.org/](https://doi.org/10.1175/JAS3614.1)
774 [10.1175/JAS3614.1](https://doi.org/10.1175/JAS3614.1).

775 Bryan, G. H., 2008: On the Computation of Pseudoadiabatic Entropy and Equivalent Potential
776 Temperature. *Mon. Wea. Rev.*, **136**, 5239–5245, <https://doi.org/10.1175/2008MWR2593.1>.

777 Bryan, G. H., and J. M. Fritsch, 2002: A Benchmark Simulation for Moist Nonhydrostatic
778 Numerical Models. *Mon. Wea. Rev.*, **130**, 2917–2928, [https://doi.org/10.1175/1520-0493\(2002\)](https://doi.org/10.1175/1520-0493(2002)130<2917:ABSFMN>2.0.CO;2)
779 [130<2917:ABSFMN>2.0.CO;2](https://doi.org/10.1175/1520-0493(2002)130<2917:ABSFMN>2.0.CO;2).

780 Bryan, G. H., and R. Rotunno, 2009: The Maximum Intensity of Tropical Cyclones in Ax-
781 isymmetric Numerical Model Simulations. *Mon. Wea. Rev.*, **137**, 1770–1789, [https://doi.org/](https://doi.org/10.1175/2008MWR2709.1)
782 [10.1175/2008MWR2709.1](https://doi.org/10.1175/2008MWR2709.1).

- 783 Cadieux, C., and Coauthors, 2022: TOI-1452 b: SPIRou and TESS Reveal a Super-Earth in a
784 Temperate Orbit Transiting an M4 Dwarf. *The Astrophysical Journal*, **164**, 96, [https://doi.org/](https://doi.org/10.3847/1538-3881/ac7cea)
785 10.3847/1538-3881/ac7cea.
- 786 Cadieux, C., and Coauthors, 2024: New Mass and Radius Constraints on the LHS 1140 planets:
787 LHS 1140 b Is either a Temperate Mini-Neptune or a Water World. *The Astrophysical Journal*
788 *Letters*, **960**, L3, <https://doi.org/10.3847/2041-8213/ad1691>.
- 789 Cesana, G., K. Suselj, and F. Brient, 2017: On the dependence of cloud feedbacks on physical
790 parameterizations in WRF aquaplanet simulations. *Geophys. Res. Lett.*, **44**, 10 762–10 771,
791 <https://doi.org/10.1002/2017GL074820>.
- 792 Changeat, Q., B. Edwards, A. F. Al-Refaie, A. Tsiaras, I. P. Waldmann, and G. Tinetti, 2019:
793 Disentangling atmospheric compositions of K2-18 b with next generation facilities. *Exp. Astron.*,
794 **53**, 391–416, <https://doi.org/10.1007/s10686-021-09794-w>.
- 795 Cronin, T. W., and D. R. Chavas, 2019: Dry and Semidry Tropical Cyclones. *J. Atmos. Sci.*, **76**,
796 2193–2212, <https://doi.org/10.1175/JAS-D-18-0357.1>.
- 797 Dauhut, T., J.-P. Chaboureaud, P. Mascart, and O. Pauluis, 2017: The Atmospheric Over-
798 turning Induced by Hector the Convecton. *J. Atmos. Sci.*, **74**, 3271–3284, [https://doi.org/](https://doi.org/10.1175/JAS-D-17-0035.1)
799 10.1175/JAS-D-17-0035.1.
- 800 Ding, F., and R. T. Pierrehumbert, 2016: Convection in Condensable-Rich Atmospheres. *The*
801 *Astrophysical Journal*, **822**, 24, <https://doi.org/10.3847/0004-637X/822/1/24>.
- 802 Dunion, J. P., 2011: Rewriting the Climatology of the Tropical North Atlantic and Caribbean Sea
803 Atmosphere. *J. Climate*, **24**, 893–908, <https://doi.org/10.1175/2010JCLI3496.1>.
- 804 Eitzen, Z. A., K. Xu, and T. Wong, 2009: Cloud and Radiative Characteristics of Tropical Deep
805 Convective Systems in Extended Cloud Objects from CERES Observations. *J. Climate*, **22**,
806 5983–6000, <https://doi.org/10.1175/2009JCLI3038.1>.
- 807 Emanuel, K. A., and M. Bister, 1996: Moist convective velocity and buoyancy scales. *J. Atmos.*
808 *Sci.*, **53**, 3276–3285, [https://doi.org/10.1175/1520-0469\(1996\)053<3276:MCVABS>2.0.CO;2](https://doi.org/10.1175/1520-0469(1996)053<3276:MCVABS>2.0.CO;2).

809 Evans, D. A., N. J. Beukes, and J. L. Kirschvink, 1997: Low-latitude glaciation in the Palaeopro-
810 terozoic era. *Nature*, **386**, 262–266, <https://doi.org/10.1038/386262a0>.

811 Fan, B., Z. Tan, T. A. Shaw, and E. S. Kite, 2021: Reducing Surface Wetness Leads to Tropical Hy-
812 drological Cycle Regime Transition. *Geophys. Res. Lett.*, **48**, e2020GL090746, [https://doi.org/](https://doi.org/10.1029/2020GL090746)
813 [10.1029/2020GL090746](https://doi.org/10.1029/2020GL090746).

814 Fang, J., O. Pauluis, and F. Zhang, 2019: The Thermodynamic Cycles and Associated Ener-
815 getics of Hurricane Edouard (2014) during Its Intensification. *J. Atmos. Sci.*, **76**, 1769–1784,
816 <https://doi.org/10.1175/JAS-D-18-0221.1>.

817 Goff, J. A., and S. Gratch, 1946: Low-pressure properties of water from -160 to 212 f, in
818 Transactions of the American Society of Heating and Ventilating Engineers, presented at the
819 52nd annual meeting of the American Society of Heating and Ventilating Engineers. 95–122.

820 Grabowski, W. W., and M. W. Moncrieff, 2004: Moisture–convection feedback in the tropics.
821 *Quart. J. Roy. Meteor. Soc.*, **130**, 3081–3104, <https://doi.org/10.1256/qj.03.135>.

822 Grell, G. A., J. Dudhia, and D. R. Stauffer, 1994: A description of the fifth-generation Penn
823 State/NCAR Mesoscale Model (MM5). Tech. rep., NCAR Tech. Note NCAR TN-398-1-STR.

824 Hartmann, D. L., and K. Larson, 2002: An important constraint on tropical cloud - climate
825 feedback. *Geophys. Res. Lett.*, **29**, 1951, <https://doi.org/10.1029/2002GL015835>.

826 Hoffman, P. F., A. J. Kaufman, G. P. Halverson, and D. P. Schrag, 1998: A Neoproterozoic
827 Snowball Earth. *Science*, **281**, 1342–1346, <https://doi.org/10.1126/science.281.5381.1342>.

828 Hong, S.-Y., Y. Noh, and J. Dudhia, 2006: A New Vertical Diffusion Package with an Explicit
829 Treatment of Entrainment Processes. *Mon. Wea. Rev.*, **134**, 2318–2341, [https://doi.org/10.1175/](https://doi.org/10.1175/MWR3199.1)
830 [MWR3199.1](https://doi.org/10.1175/MWR3199.1).

831 Hong, S.-Y., and H. Pan, 1996: Nonlocal Boundary Layer Vertical Diffusion in a Medium-Range
832 Forecast Model. *Mon. Wea. Rev.*, **124**, 2322–2339, [https://doi.org/10.1175/1520-0493\(1996\)](https://doi.org/10.1175/1520-0493(1996)124(2322:NBLVDI)2.0.CO;2)
833 [124\(2322:NBLVDI\)2.0.CO;2](https://doi.org/10.1175/1520-0493(1996)124(2322:NBLVDI)2.0.CO;2).

834 Hueso, R., and A. Sánchez-Lavega, 2006: Methane storms on Saturn’s moon Titan. *Nature*, **442**,
835 428–431, <https://doi.org/10.1038/nature04933>.

- 836 Igel, M. R., A. J. Drager, and S. C. van den Heever, 2014: A CloudSat cloud object partitioning
837 technique and assessment and integration of deep convective anvil sensitivities to sea surface tem-
838 perature. *J. Geophys. Res. Atmos.*, **119**, 10 515–10 535, <https://doi.org/10.1002/2014JD021717>.
- 839 Jeevanjee, N., and D. M. Romps, 2013: Convective self-aggregation, cold pools, and domain size.
840 *Geophys. Res. Lett.*, **40**, 994–998, <https://doi.org/10.1002/grl.50204>.
- 841 Jiménez, P. A., J. Dudhia, J. F. González-Rouco, J. Navarro, J. P. Montávez, and E. García-
842 Bustamante, 2012: A Revised Scheme for the WRF Surface Layer Formulation. *Mon. Wea.*
843 *Rev.*, **140**, 898–918, <https://doi.org/10.1175/MWR-D-11-00056.1>.
- 844 Kasting, J. F., 1988: Runaway and moist greenhouse atmospheres and the evolution of Earth and
845 Venus. *Icarus*, **74**, 472–494, [https://doi.org/10.1016/0019-1035\(88\)90116-9](https://doi.org/10.1016/0019-1035(88)90116-9).
- 846 Khairoutdinov, M. F., and K. A. Emanuel, 2013: Rotating radiative-convective equilibrium simu-
847 lated by a cloud-resolving model. *Journal of Advances in Modeling Earth Systems*, **5**, 816–825,
848 <https://doi.org/10.1002/2013MS000253>.
- 849 Kirschvink, J. L., 1992: *Late Proterozoic low-latitude global glaciation: the snowball Earth.*
850 *In: The Proterozoic biosphere: A multidisciplinary study [Schopf, J. and C. Klein (eds.)]*,
851 51–52. Cambridge University Press, Cambridge, United Kingdom and New York, NY, USA,
852 <https://doi.org/10.1017/CBO9780511601064>.
- 853 Kuang, Z., and D. L. Hartmann, 2007: Testing the Fixed Anvil Temperature Hypothesis in a
854 Cloud-Resolving Model. *J. Climate*, **20**, 2051–2057, <https://doi.org/10.1175/JCLI4124.1>.
- 855 Li, C., and A. Ingersoll, 2015: Moist convection in hydrogen atmospheres and the frequency of
856 Saturn’s giant storms. *Nature Geosci.*, **8**, 398–403, <https://doi.org/10.1038/ngeo2405>.
- 857 Li, Y., Y. Wang, and Z.-M. Tan, 2023: Is the outflow-layer inertial stability crucial to
858 the energy cycle and development of tropical cyclones? *J. Atmos. Sci.*, <https://doi.org/10.1175/JAS-D-22-0186.1>.
- 859
- 860 Madhusudhan, N., M. C. Nixon, L. Welbanks, A. A. A. Piette, and R. A. Booth, 2020: The Interior
861 and Atmosphere of the Habitable-zone Exoplanet K2-18b. *The Astrophysical Journal Letters*,
862 **891**, L7, <https://doi.org/10.3847/2041-8213/ab7229>.

- 863 Mahrt, L. T., and J. Sun, 1995: The subgrid velocity scale in the bulk aerodynamic relationship
864 for spatially averaged scalar fluxes. *Mon. Wea. Rev.*, **123**, 3032–3041, [https://doi.org/10.1175/
865 1520-0493\(1995\)123\(3032:TSVSIT\)2.0.CO;2](https://doi.org/10.1175/1520-0493(1995)123(3032:TSVSIT)2.0.CO;2).
- 866 Mansell, E., and C. L. Ziegler, 2010: Aerosol Effects on Simulated Storm Electrification and
867 Precipitation in a Two-Moment Bulk Microphysics Model. *J. Atmos. Sci.*, **70**, 2032–2050,
868 <https://doi.org/10.1175/JAS-D-12-0264.1>.
- 869 Mansell, E., C. L. Ziegler, and E. C. Bruning, 2010: Simulated Electrification of a Small Thun-
870 derstorm with Two-Moment Bulk Microphysics. *J. Atmos. Sci.*, **67**, 171–194, [https://doi.org/
871 10.1175/2009JAS2965.1](https://doi.org/10.1175/2009JAS2965.1).
- 872 Marquet, P., 2011: Definition of a moist entropy potential temperature: application to FIRE-I data
873 flights. *Quart. J. Roy. Meteor. Soc.*, **137**, 768–791, <https://doi.org/10.1002/qj.787>.
- 874 Marquet, P., 2017: A third-law isentropic analysis of a simulated hurricane. *J. Atmos. Sci.*, **74**,
875 3451–3471, <https://doi.org/10.1175/JAS-D-17-0126.1>.
- 876 McColl, K. A., and L. I. Tang, 2024: An Analytic Theory of Near-Surface Relative Humidity over
877 Land. *J. Climate*, **37**, 1213–1230, <https://doi.org/10.1175/JCLI-D-23-0342.1>.
- 878 McKinney, M. M., and J. Mitchell, 2024: Seasons, Shorelines, and Their Effects on the Tropical
879 Circulation and Hydrological Cycle. *J. Atmos. Sci.*, **81**, 1475–1494, [https://doi.org/10.1175/
880 JAS-D-23-0076.1](https://doi.org/10.1175/JAS-D-23-0076.1).
- 881 McKinney, M. M., J. Mitchell, and S. I. Thomson, 2022: Effects of Varying Land Coverage,
882 Rotation Period, and Water Vapor on Equatorial Climates that Bridge the Gap between Earth-
883 like and Titan-like. *J. Atmos. Sci.*, **79**, 2813–2830, <https://doi.org/10.1175/JAS-D-21-0295.1>.
- 884 Mikal-Evans, T., N. Madhusudhan, J. Dittmann, M. N. Günther, L. Welbanks, V. V. Eyles, I. J.
885 M. C. T. Daylan, and L. Kreidberg, 2023: Hubble Space Telescope Transmission Spectroscopy
886 for the Temperate Sub-Neptune TOI-270 d: A Possible Hydrogen-rich Atmosphere Containing
887 Water Vapor. *The Astronomical Journal*, **165**, 84, <https://doi.org/10.3847/1538-3881/aca90b>.
- 888 Mitchell, J., 2008: The drying of Titan’s dunes: Titan’s methane hydrology and its impact on
889 atmospheric circulation. *J. Geophys. Res.*, **113**, E08 015, <https://doi.org/10.1029/2007JE003017>.

- 890 Mitchell, J., and J. M. Lora, 2016: The Climate of Titan. *Annual Review of Earth and Planetary*
891 *Sciences*, **44**, 353–380, <https://doi.org/10.1146/annurev-earth-060115-012428>.
- 892 Mitchell, J., R. Pierrehumbert, D. Frierson, and R. Caballero, 2006: The dynamics behind Titan’s
893 methane clouds. *Proc. Natl. Acad. Sci. (USA)*, **103**, 18 421–18 426, [https://doi.org/10.1073/pnas.](https://doi.org/10.1073/pnas.0605074103)
894 [0605074103](https://doi.org/10.1073/pnas.0605074103).
- 895 Mitchell, J., R. Pierrehumbert, D. Frierson, and R. Caballero, 2009: The impact of methan
896 thermodynamics on seasonal convection and circulation in a model Titan atmosphere. *Icarus*,
897 **203**, 250–264, <https://doi.org/10.1016/j.icarus.2009.03.043>.
- 898 Morrison, H., J. A. Curry, and V. I. Khvorostyanov, 2005: A New Double-Moment Microphysics
899 Parameterization for Application in Cloud and Climate Models. Part I: Description. *J. Atmos.*
900 *Sci.*, **62**, 1665–1677, <https://doi.org/10.1175/JAS3446.1>.
- 901 Morrison, H., G. Thompson, and V. Tatarskii, 2009: Impact of Cloud Microphysics on the
902 Development of Trailing Stratiform Precipitation in a Simulated Squall Line: Comparison of
903 One- and Two-Moment Schemes. *Mon. Wea. Rev.*, **137**, 991–1007, [https://doi.org/10.1175/](https://doi.org/10.1175/2008MWR2556.1)
904 [2008MWR2556.1](https://doi.org/10.1175/2008MWR2556.1).
- 905 Mrowiec, A. A., S. T. Garner, and O. M. Pauluis, 2011: Axisymmetric Hurricane in a Dry
906 Atmosphere: Theoretical Framework and Numerical Experiments. *J. Atmos. Sci.*, **68**, 1607–
907 1619, <https://doi.org/10.1175/2011JAS3639.1>.
- 908 Mrowiec, A. A., O. M. Pauluis, A. M. Frindlind, and A. S. Ackerman, 2015: Properties of a
909 Mesoscale Convective System in the Context of an Isentropic Analysis. *J. Atmos. Sci.*, **72**,
910 1945–1962, <https://doi.org/10.1175/JAS-D-14-0139.1>.
- 911 Mrowiec, A. A., O. M. Pauluis, and F. Zhang, 2016: Isentropic Analysis of a Simulated Hurricane.
912 *J. Atmos. Sci.*, **73**, 1857–1870, <https://doi.org/10.1175/JAS-D-15-0063.1>.
- 913 Muller, C. J., and I. M. Held, 2012: Detailed Investigation of the Self-Aggregation of Con-
914 vection in Cloud-Resolving Simulations. *J. Atmos. Sci.*, **69**, 2551–2565, [https://doi.org/](https://doi.org/10.1175/JAS-D-11-0257.1)
915 [10.1175/JAS-D-11-0257.1](https://doi.org/10.1175/JAS-D-11-0257.1).

- 916 Muller, C. J., and D. M. Romps, 2018: Acceleration of tropical cyclogenesis by self-
917 aggregation feedbacks. *Proc. Natl. Acad. Sci. (USA)*, **115**, 2930–2935, [https://doi.org/10.1073/](https://doi.org/10.1073/pnas.1719967115)
918 [pnas.1719967115](https://doi.org/10.1073/pnas.1719967115).
- 919 Nakanishi, M., and H. Niino, 2006: An Improved Mellor–Yamada Level-3 Model: Its Numerical
920 Stability and Application to a Regional Prediction of Advection Fog. *Boundary-Layer Meteorol.*,
921 **119**, 397–407, <https://doi.org/10.1007/s10546-005-9030-8>.
- 922 Nakanishi, M., and H. Niino, 2009: Development of an Improved Turbulence Closure Model
923 for the Atmospheric Boundary Layer. *J. Meteor. Soc. Japan*, **87**, 895–912, [https://doi.org/](https://doi.org/10.2151/jmsj.87.895)
924 [10.2151/jmsj.87.895](https://doi.org/10.2151/jmsj.87.895).
- 925 Núñez Ocasio, K. M., and E. M. Dougherty, 2024: The effect of pseudo-global warming on the
926 weather-climate system of Africa in a convection-permitting model. *Geophys. Res. Lett.*, **51**,
927 [e2024GL112341](https://doi.org/10.1029/2024GL112341), <https://doi.org/10.1029/2024GL112341>.
- 928 Ohno, T., and M. Satoh, 2018: Roles of cloud microphysics on cloud responses to sea sur-
929 face temperatures in radiative-convective equilibrium experiments using a high-resolution
930 global nonhydrostatic model. *J. Adv. Model. Earth Syst.*, **10**, 1970–1989, [https://doi.org/](https://doi.org/10.1029/2018MS001386)
931 [10.1029/2018MS001386](https://doi.org/10.1029/2018MS001386).
- 932 Olson, J. B., J. S. Kenyon, W. M. Angevine, J. M. . Brown, M. Pagowski, and K. Sušelj, 2019: A De-
933 scription of the MYNN-EDMF Scheme and the Coupling to Other Components in WRF–ARW.
934 *NOAA Technical Memorandum OAR GSD*, **61**, 37, <https://doi.org/10.25923/n9wm-be49>.
- 935 O’Neill, M., and D. R. Chavas, 2020: Inertial Waves in Axisymmetric Tropical Cyclones. *J. Atmos.*
936 *Sci.*, **77**, 2501–2517, <https://doi.org/10.1175/JAS-D-19-0330.1>.
- 937 Pauluis, O., and I. M. Held, 2002a: Entropy Budget of an Atmosphere in Radiative–Convective
938 Equilibrium. Part I: Maximum Work and Frictional Dissipation. *J. Atmos. Sci.*, **59**, 125–139,
939 [https://doi.org/10.1175/1520-0469\(2002\)059<0125:EBOAAI>2.0.CO;2](https://doi.org/10.1175/1520-0469(2002)059<0125:EBOAAI>2.0.CO;2).
- 940 Pauluis, O., and I. M. Held, 2002b: Entropy Budget of an Atmosphere in Radiative–Convective
941 Equilibrium. Part II: Latent Heat Transport and Moist Processes. *J. Atmos. Sci.*, **59**, 140–149,
942 [https://doi.org/10.1175/1520-0469\(2002\)059<0140:EBOAAI>2.0.CO;2](https://doi.org/10.1175/1520-0469(2002)059<0140:EBOAAI>2.0.CO;2).

- 943 Pauluis, O. M., 2000: Entropy budget of an atmosphere in radiative–convective equilibrium. Ph.D.
944 thesis, Princeton University.
- 945 Pauluis, O. M., 2011: Water Vapor and Mechanical Work: A Comparison of Carnot and Steam
946 Cycles. *J. Atmos. Sci.*, **68**, 91–102, <https://doi.org/10.1175/2010JAS3530.1>.
- 947 Pauluis, O. M., 2016: The Mean Air Flow as Lagrangian Dynamics Approximation and Its
948 Application to Moist Convection. *J. Atmos. Sci.*, **73**, 4407–4425, [https://doi.org/10.1175/
949 JAS-D-15-0284.1](https://doi.org/10.1175/JAS-D-15-0284.1).
- 950 Pauluis, O. M., and A. A. Mrowiec, 2013: Isentropic Analysis of Convective Motions. *J. Atmos.*
951 *Sci.*, **70**, 3673–3688, <https://doi.org/10.1175/JAS-D-12-0205.1>.
- 952 Pauluis, O. M., and F. Zhang, 2017: Reconstruction of Thermodynamic Cycles in a High-
953 Resolution Simulation of a Hurricane. *J. Atmos. Sci.*, **74**, 3367–3381, [https://doi.org/10.1175/
954 JAS-D-16-0353.1](https://doi.org/10.1175/JAS-D-16-0353.1).
- 955 Piaulet, C., and Coauthors, 2023: Evidence for the volatile-rich composition of a 1.5-Earth-radius
956 planet. *Nat. Astron.*, **7**, 206–222, <https://doi.org/10.1038/s41550-022-01835-4>.
- 957 Piaulet-Ghorayeb, C., and Coauthors, 2024: JWST/NIRISS Reveals the Water-rich ”Steam World”
958 Atmosphere of GJ 9827 d. *The Astrophysical Journal Letters*, **974**, L10, [https://doi.org/10.3847/
959 2041-8213/ad6f00](https://doi.org/10.3847/2041-8213/ad6f00).
- 960 Pierrehumbert, R. T., and F. Ding, 2016: Dynamics of atmospheres with a non-dilute conden-
961 sible component. *Proc. Roy. Soc. A: Mathematical, Physical and Engineering Sciences*, **472**,
962 20160107, <https://doi.org/10.1098/rspa.2016.0107>.
- 963 Régibeau-Rockett, L., 2025: Thermodynamic behavior of atmospheric heat engines in different
964 environments. Ph.D. thesis, Stanford University.
- 965 Régibeau-Rockett, L., O. M. Pauluis, and M. E. O’Neill, 2024: Investigating the Relationship
966 between Sea Surface Temperature and the Mechanical Efficiency of Tropical Cyclones. *J.*
967 *Climate*, **37**, 439–456, <https://doi.org/10.1175/JCLI-D-22-0877.1>.

968 Rennó, N. O., and A. P. Ingersoll, 1996: Natural convection as a heat engine: A theory for CAPE.
969 *J. Atmos. Sci.*, **53**, 572–585, [https://doi.org/10.1175/1520-0469\(1996\)053<0572:NCAAHE>2.0.](https://doi.org/10.1175/1520-0469(1996)053<0572:NCAAHE>2.0.CO;2)
970 CO;2.

971 Rochetin, N., B. R. Lintner, K. L. Findell, A. H. Sobel, and P. Gentine, 2014: Radiative–Convective Equilibrium over a Land Surface. *J. Climate*, **27**, 8611–8629, <https://doi.org/10.1175/JCLI-D-13-00654.1>.

974 Roy, P.-A., and Coauthors, 2023: Water Absorption in the Transmission Spectrum of the Water
975 World Candidate GJ 9827 d. *The Astrophysical Journal Letters*, **954**, L52, <https://doi.org/10.3847/2041-8213/acebf0>.

977 Satoh, M., S. Iga, H. Tomita, Y. Tsushima, and A. T. Noda, 2012: Response of Upper Clouds
978 in Global Warming Experiments Obtained Using a Global Nonhydrostatic Model with Explicit
979 Cloud Processes. *J. Clim.*, **25**, 2178–2191, <https://doi.org/10.1175/JCLI-D-11-00152.1>.

980 Seeley, J. T., N. Jeevanjee, and D. M. Romps, 2019: FAT or FiTT: Are anvil clouds or the
981 tropopause temperature invariant? *Geophys. Res. Lett.*, **46**, 1842–1850, [https://doi.org/10.1029/](https://doi.org/10.1029/2018GL080096)
982 2018GL080096.

983 Seidel, D. J., Y. Zhang, A. Beljaars, J.-C. Golaz, A. R. Jacobson, and B. Medeiros, 2012: Climatol-
984 ogy of the planetary boundary layer over the continental United States and Europe. *J. Geophys.*
985 *Res.*, **117**, D17 106, <https://doi.org/10.1029/2012JD018143>.

986 Singh, M. S., and P. A. O’Gorman, 2015: Increases in moist-convective updraught velocities
987 with warming in radiative-convective equilibrium. *Quart. J. Roy. Meteor. Soc.*, **141**, 2828–2838,
988 <https://doi.org/10.1002/qj.2567>.

989 Singh, M. S., and P. A. O’Gorman, 2016: Scaling of the entropy budget with surface temperature
990 in radiative-convective equilibrium. *Journal of Advances in Modeling Earth Systems*, **8**, 1132–
991 1150, <https://doi.org/10.1002/2016MS000673>.

992 Singh, M. S., and M. E. O’Neill, 2022: The climate system and the second law of thermodynamics.
993 *Rev. Mod. Phys.*, **94**, 015 001, <https://doi.org/10.1103/RevModPhys.94.015001>.

994 Skamarock, W. C., and Coauthors, 2008: A description of the advanced research WRF version 3.
995 Tech. rep., National Center for Atmospheric Research, Boulder, Colorado, USA.

- 996 Southworth, J., L. Mancini, N. Madhusudhan, P. Mollière, S. Ciceri, and T. Henning, 2017:
997 Detection of the Atmosphere of the 1.6 M_⊕ Exoplanet GJ 1132 b. *The Astronomical Journal*,
998 **153**, 191, <https://doi.org/10.3847/1538-3881/aa6477>.
- 999 Spaulding-Astudillo, F. E., and J. L. Mitchell, 2023: Effects of Varying Saturation Vapor Pressure
1000 on Climate, Clouds, and Convection. *J. Atmos. Sci.*, **80**, 1247–1266, [https://doi.org/10.1175/
1001 JAS-D-22-0063.1](https://doi.org/10.1175/JAS-D-22-0063.1).
- 1002 Thompson, D. W. J., S. Bony, and Y. Li, 2017: Thermodynamic constraint on the depth of the
1003 global tropospheric circulation. *Proc. Natl. Acad. Sci. (USA)*, **114**, 8181–8186, [https://doi.org/
1004 10.1073/pnas.1620493114](https://doi.org/10.1073/pnas.1620493114).
- 1005 Thompson, G., and T. Eidhammer, 2014: A Study of Aerosol Impacts on Clouds and Precipitation
1006 Development in a Large Winter Cyclone. *J. Atmos. Sci.*, **71**, 3636–3658, [https://doi.org/10.1175/
1007 JAS-D-13-0305.1](https://doi.org/10.1175/JAS-D-13-0305.1).
- 1008 Thompson, G., P. R. Field, R. M. Rasmussen, and W. D. Hall, 2008: Explicit Forecasts of
1009 Winter Precipitation Using an Improved Bulk Microphysics Scheme. Part II: Implementation
1010 of a New Snow Parameterization. *Mon. Wea. Rev.*, **136**, 5095–5115, [https://doi.org/10.1175/
1011 2008MWR2387.1](https://doi.org/10.1175/2008MWR2387.1).
- 1012 Thuburn, J., and G. C. Craig, 2002: On the temperature structure of the tropical stratosphere.
1013 *J. Geophys. Res.*, **107**, <https://doi.org/10.1029/2001JD000448>.
- 1014 Tobin, I., S. Bony, and R. Roca, 2012: Observational Evidence for Relationships between the
1015 Degree of Aggregation of Deep Convection, Water Vapor, Surface Fluxes, and Radiation. *J.
1016 Climate*, **25**, 6885–6904, <https://doi.org/10.1175/JCLI-D-11-00258.1>.
- 1017 Tompkins, A. M., and A. G. Semie, 2017: Organization of tropical convection in low vertical wind
1018 shears: Role of updraft entrainment. *J. Adv. Model. Earth Syst.*, **9**, 1046–1068, [https://doi.org/
1019 10.1002/2016MS000802](https://doi.org/10.1002/2016MS000802).
- 1020 Tsiaras, A., I. P. Waldmann, G. Tinetti, J. Tennyson, and S. N. Yurchenko, 2019: Water vapour in the
1021 atmosphere of the habitable-zone eight-Earth-mass planet K2-18 b. *Nat. Astron.*, **3**, 1086–1091,
1022 <https://doi.org/10.1038/s41550-019-0878-9>.

- 1023 Tsushima, Y., S. Iga, H. Tomita, M. Satoh, A. T. Noda, and M. J. Webb, 2014: High cloud increase
1024 in a perturbed SST experiment with a global nonhydrostatic model including explicit convective
1025 processes. *J. Adv. Model. Earth Syst.*, **6**, 571–585, <https://doi.org/10.1002/2013MS000301>.
- 1026 Urata, R. A., and O. B. Toon, 2013: Simulations of the martian hydrologic cycle with a gen-
1027 eral circulation model: Implications for the ancient martian climate. *Icarus*, **226**, 229–250,
1028 <https://doi.org/10.1016/j.icarus.2013.05.014>.
- 1029 van der Drift, R. T., and P. A. O’Gorman, 2025: Dependence of Convective Precipitation
1030 Extremes on Near-Surface Relative Humidity. *J. Climate*, **38**, 6207–6225, <https://doi.org/10.1175/JCLI-D-24-0738.1>.
- 1032 von Engel, A., and J. Teixeira, 2013: A Planetary Boundary Layer Height Climatol-
1033 ogy Derived from ECMWF Reanalysis Data. *J. Climate*, **26**, 6575–6590, <https://doi.org/10.1175/JCLI-D-12-00385.1>.
- 1035 Wang, D., and Y. Lin, 2020: Size and Structure of Dry and Moist Reversible Tropical Cyclones.
1036 *J. Atmos. Sci.*, **77**, 2091–2114, <https://doi.org/10.1175/JAS-D-19-0229.1>.
- 1037 Wang, D., and Y. Lin, 2021: Potential Role of Irreversible Moist Processes in Modulat-
1038 ing Tropical Cyclone Surface Wind Structure. *J. Atmos. Sci.*, **78**, 709–725, <https://doi.org/10.1175/JAS-D-20-0192.1>.
- 1040 Wilhelmson, R. B., and C.-S. Chen, 1982: A Simulation of the Development of Successive
1041 Cells Along a Cold Outflow Boundary. *J. Atmos. Sci.*, **39**, 1466–1483, [https://doi.org/10.1175/1520-0469\(1982\)039<1466:ASOTDO>2.0.CO;2](https://doi.org/10.1175/1520-0469(1982)039<1466:ASOTDO>2.0.CO;2).
- 1043 Wing, A. A., and T. W. Cronin, 2016: Self-aggregation of convection in long channel geometry.
1044 *Quart. J. Roy. Meteor. Soc.*, **142**, 1–15, <https://doi.org/10.1002/qj.2628>.
- 1045 WMO, 1957: Meteorology-A three-dimensional science: Second session of the commission for
1046 aerology. *WMO Bull.*, **4**, 134–138.
- 1047 Wordsworth, R., F. Forget, E. Millour, J. W. Head, J.-B. Madeleine, and B. Charnay, 2013: Global
1048 modelling of the early martian climate under a denser CO₂ atmosphere: Water cycle and ice
1049 evolution. *Icarus*, **222**, 1–19, <https://doi.org/10.1016/j.icarus.2012.09.036>.

- 1050 Xian, T., and C. R. Homeyer, 2019: Global tropopause altitudes in radiosondes and reanalyses.
1051 *Atmos. Chem. Phys.*, **19**, 5661–5678, <https://doi.org/10.5194/acp-19-5661-2019>.
- 1052 Xu, K., T. Wong, B. A. Wielicki, L. Parker, and Z. A. Eitzen, 2005: Statistical Analyses of Satellite
1053 Cloud Object Data from CERES. Part I: Methodology and Preliminary Results of the 1998 El
1054 Niño/2000 La Niña. *J. Climate*, **18**, 2497–2514, <https://doi.org/10.1175/JCLI3418.1>.
- 1055 Zelinka, M. D., and D. L. Hartmann, 2010: Why is longwave cloud feedback positive? *J. Geophys.*
1056 *Res.*, **115**, D16 117, <https://doi.org/10.1029/2010JD013817>.
- 1057 Zhang, Y., K. Sun, Z. Gao, Z. Pan, M. A. Shook, and D. Li, 2020: Diurnal climatology of planetary
1058 boundary layer height over the contiguous United States derived from AMDAR and reanalysis
1059 data. *J. Geophys. Res. Atmos.*, **125**, e2020JD032 803, <https://doi.org/10.1029/2020JD032803>.
- 1060 Ziegler, C. L., 1985: Retrieval of Thermal and Microphysical Variables in Observed Convective
1061 Storms. Part 1: Model Development and Preliminary Testing. *J. Atmos. Sci.*, **42**, 1487–1509,
1062 [https://doi.org/10.1175/1520-0469\(1985\)042<1487:ROTAMV>2.0.CO;2](https://doi.org/10.1175/1520-0469(1985)042<1487:ROTAMV>2.0.CO;2).
- 1063 Zsom, A., L. Kaltenecker, and C. Goldblatt, 2012: A 1d microphysical cloud model for Earth, and
1064 Earth-like exoplanets: Liquid water and water ice clouds in the convective troposphere. *Icarus*,
1065 **221**, 603–616, <https://doi.org/10.1016/j.icarus.2012.08.028>.